Contemporary Mathematics
https://ojs.wiserpub.com/index.php/CM/

Research Article

Thermal-Mechanical Coupling Response Analysis of Three-layer Circular and Horseshoe Shaped Chambers Based on Complex Elastic Mechanics

Fuqing Li[1,2,7], Jianjie Zheng[1,3], Rui Sun[4*], Fufeng Li[5], Lan Shen[6], Yukun Ji[1], Yan Shen[6,7], Ya Shi[8], Yun Wu[1]

[1] State Key Laboratory of Intelligent Construction and Healthy Operation and Maintenance of Deep Underground Engineering, China University of Mining and Technology, Xuzhou, 221116, China
[2] Yunlong Lake Laboratory of Deep Underground Science and Engineering, Xuzhou, 221116, China
[3] Shanghai Municipal Safety and Quality Supervision Administration for Construction Engineering, Shanghai, 200032, China
[4] School of Mechanics and Civil Engineering, China University of Mining and Technology, Xuzhou, 221116, China
[5] Shanghai Urban Construction Municipal Engineering (Group) Co., Ltd., Shanghai, 200232, China
[6] Shanghai Tunnel Engineering Co., Ltd, Shanghai, 200032, China
[7] Shanghai Clean Tunnel Engineering Technology Co., Ltd., Shanghai, 201101, China
[8] Hefei Deep Underground Space Technology Center, Hefei, 230000, China
E-mail: sunrui@cumt.edu.cn

Received: 20 May 2025; **Revised:** 28 May 2025; **Accepted:** 30 May 2025

Abstract: Compressed Air Energy Storage (CAES) in abandoned coal mines offers a cost-effective and sustainable solution for large-scale energy storage. This study presents a comprehensive analytical framework to evaluate the thermo-mechanical behavior and long-term structural stability of three-layer underground chambers with circular and horseshoe-shaped cross-sections. Based on the theory of complex elasticity and conformal mapping, analytical solutions for stress and displacement are derived under steady-state thermal conditions. The framework incorporates both mechanical loads-such as in-situ stress and internal gas pressure-and temperature-induced thermal stresses, which are often overlooked in traditional models. Using the Cao Zhuang Coal Mine in Shandong Province as a case study, the analytical results are validated against finite element simulations performed in COMSOL 6.2. The validation demonstrates strong agreement in both temperature and stress distributions across different burial depths. Comparative results reveal that while circular chambers maintain relatively uniform stress profiles, horseshoe-shaped chambers are prone to localized stress concentrations, especially near the lower arch and corner regions. This makes them more vulnerable to structural failure under thermal cycling conditions. The findings underscore the importance of incorporating thermal effects in underground energy storage system design. The developed methodology offers a computationally efficient alternative to fully numerical simulations, enabling rapid scenario assessment and structural optimization. This work provides theoretical and practical insights into the safe reuse of abandoned mine tunnels for energy storage, contributing to the long-term feasibility of compressed air energy storage systems and the advancement of clean energy infrastructure.

***Keywords*:** Compressed Air Energy Storage (CAES), circular chamber, horseshoe shaped chamber, thermal-mechanical coupling, analytical solution

MSC: 74F05, 30E25

DOI: https://doi.org/10.37256/cm.6420257277

1. Introduction

With the transition toward renewable energy and the modernization of power systems, Compressed Air Energy Storage (CAES) has emerged as a key solution for large-scale energy storage, providing critical support for grid stability [1]. The concept of repurposing abandoned coal mines as CAES reservoirs has gained increasing attention due to their extensive underground space, which offers a cost-effective and environmentally friendly storage alternative [2]. Compared to conventional energy storage methods, CAES exhibits advantages such as high energy density, long cycle life, and minimal environmental impact [3]. Unlike lithium-ion batteries and flow batteries, CAES does not rely on rare metals or toxic chemicals, significantly reducing the risk of environmental contamination during production, use, and disposal. Furthermore, unlike pumped hydro storage, CAES systems require less surface land and can be deployed in existing subsurface spaces, such as abandoned coal mines, thereby avoiding additional ecological disturbance. The reuse of abandoned mine infrastructure further enhances sustainability by minimizing construction demands and preserving land resources. However, the deployment of CAES in abandoned coal mines presents significant engineering challenges, requiring a comprehensive investigation into the mechanical and thermal behaviors of underground storage chambers [4].

Globally, CAES projects such as those in Huntorf, Germany [5], and McIntosh, USA [6], have demonstrated the feasibility of this technology. However, these facilities were constructed in engineered caverns rather than abandoned mines, where complex geological conditions introduce additional uncertainties [7]. The conversion of abandoned mines into CAES chambers necessitates a deep understanding of geomechanically stability, cyclic load fatigue, and thermal-mechanical coupling effects, all of which significantly influence long-term structural integrity. The cyclic inflation and deflation processes in CAES subject underground chambers to repeated pressurization and decompression, creating a multi-physics problem involving mechanical, thermal, and fatigue effects [8]. The structural stability of underground chambers is influenced by interactions between geostress and internal gas pressure, potentially leading to fatigue-induced degradation in sealing and lining layers over prolonged operation cycles [9]. The thermal-mechanical coupling effect further complicates stability analysis, as compressed air introduces substantial temperature variations that generate additional thermal stresses [10]. Heat transfer between the compressed air and surrounding rock alters stress distribution patterns, affecting the long-term stability of the chamber.

Table 1. Foreign compressed air energy storage projects

Year	Project name	Country	Geological conditions
1978	Huntorf project [14]	Germany	Salt cavern
1990	Kamioka project [15]	Japan	Abandoned coal mines
1991	McIntosh project [14]	America	Salt cavern
2013	Pacific northwest national laboratory project [16]	Colombia	Basalt mine
2013	Adele project [17]	Germany	Salt cavern
2013	Hebei langfang 1.5 MW Supercritical compressed air energy storage Demonstration project [18]	China	Hard rock cavern
2015	Norton CAES project [19, 20]	America	Limestone mine
2016	ALACAES project [17]	Switzerland	Abandoned tunnel
2017	Matagorda energy center project [21]	America	Salt cavern
2020	Yungang CAES project [22]	China	Abandoned coal mines
2021	Jintan salt cave CAES project [23]	China	Salt cavern
2022	Berkeley energy center project [24]	America	Salt cavern
2022	Hydrostor project [25]	Canada	Hard rock cavern

Additionally, the geometric complexity of underground chambers presents further analytical challenges. Abandoned coal mine tunnels are typically horseshoe-shaped or circular [11], necessitating distinct analytical approaches to accurately model stress responses. Conventional analytical models often oversimplify these geometries, leading to inaccuracies in stress distribution predictions [12]. Another critical aspect is air containment and leakage prevention, as the sealing and lining layers must maintain structural integrity under cyclic loading conditions [13]. Pre-existing fractures in surrounding rock formations could contribute to progressive air loss, reducing system efficiency and increasing operational risks. But with the unremitting efforts of scientific researchers, there are already many CAES projects that have been implemented, and we have summarized some of the projects as shown in Table 1.

Most existing studies on underground CAES rely heavily on Finite Element Method (FEM) simulations, which provide detailed insights into stress and deformation behavior [26]. In 2012, Kim et al. [15] proposed a model with a vertical rupture surface and provided calculation methods for the safety factors of two types of gas storage caverns: large tank and tunnel. Thongraksa et al. [27] analyzed the failure mode and showed that it was independent of the initial stress conditions, and the failure location was affected by the combined effects of strength and initial stress. Raju et al. [28] proposed an accurate thermodynamic model for compressed air energy storage chambers based on the Huntorf power station, and corrected the heat transfer coefficient. Winn et al. [29] conducted a comprehensive analysis of multiple key issues, including the safety and stability of the first commercial underground cave for hydrocarbon storage. Rutqvist et al. [30] conducted a comprehensive study on the mechanical behavior of concrete lined CAES caverns using the TOUGH-FLAC simulator. Perazzelli and Anagnostou [31] conducted an in-depth analysis of the technical feasibility of using newly excavated shallow buried hard rock gas storage chambers as CAES storage facilities under high pressures. Kushnir et al. [32] conducted an analysis and study on the thermodynamic response of compressed air in rock caves, and successfully derived analytical expressions for the changes in air temperature and pressure during typical CAES operation cycles.

Based on this, Zhou et al. [33] proposed an analytical solution to describe the mechanical response caused by changes in air pressure and temperature inside lined rock caves. Xia et al. [34] further introduced a simplified and unified analysis solution that comprehensively considers the heat exchange between compressed air and surrounding rocks, thereby accurately predicting the temperature and pressure changes inside CAES caves. Zhou et al. [35] simulated the cyclic charging and discharging process of CAES and analyzed that the air temperature and pressure in each cycle of the storage tank showed consistent changes. Wu et al. [36] developed a “hot fluid solid” model that integrates non isothermal heat transfer, air infiltration, and geomechanically deformation of surrounding rocks to simulate air leakage and development patterns in unlined caves in deep ground space. Chen and Wang [26] explored the impact of the Excavation Damage Zone (EDZ) of surrounding rock on the stability of caverns.

However, FEM models are computationally expensive and impractical for large-scale real-time applications. Traditional elasticity-based analytical models, while computationally efficient, often fail to account for thermal effects and geometrical complexities [12]. The development of single-layer cavity analysis theory began with the classical elastic mechanics framework. Kirsch [37] first established the elastic stress solution of a circular cavity in a uniform in-situ stress field, revealing the basic law of the tangential stress concentration coefficient around the cavity. Lu et al. [38] proposed an analytical model under generalized external loads, coupling the lateral pressure coefficient with the gravity field for the first time and establishing a unified expression for asymmetric loads. However, the model did not take into account the effect of internal pressure. Wang and Li [39] used the complex function method to establish a double-layer cavity model, and described the interaction between the lining and the surrounding rock through displacement coordination conditions. The interface slip coefficient introduced by them can quantitatively characterize the mechanical behavior of the contact surface. EI et al. [40] first established an elastic analytical solution for a three-layer structure and found that the internal pressure load needs to be iteratively solved through interlayer coupling equations, rather than simple boundary force treatment. Exadaktylos [41, 42] achieved the display expression of multi-layer tunnel stress by introducing a closed field solution, but it is only applicable to linear elastic materials. Sun et al. [12] used the theory of complex elasticity to establish analytical solutions for different circular chambers with different layers. The results showed that the stability of CAES chambers can be effectively and quickly evaluated through these analytical solutions and comprehensive parameters, and enhanced by materials with low bulk modulus but high shear modulus.

The development of analytical solutions for CAES chamber thermal-mechanical behavior is crucial for several reasons. First, analytical solutions provide deep physical insights into the problem, helping researchers grasp the fundamental mechanisms governing stress and deformation in underground storage systems [43]. Second, they offer significant computational efficiency compared to numerical methods, allowing for rapid parameter analysis and optimization. Additionally, analytical solutions serve as a valuable verification tool for numerical simulations, ensuring their reliability and accuracy [12]. Finally, they provide a solid theoretical foundation for engineering applications, guiding the design and construction of CAES chambers in practical settings. While study on circular chambers has been extensively conducted, studies focusing on horseshoe-shaped chambers remain relatively scarce due to their inherent mathematical complexity [44, 45]. To address these limitations, the integration of complex elasticity theory with conformal transformation techniques provides an effective means of mapping irregular geometries into computationally manageable domains, thereby improving analytical accuracy. The novelty of this study lies in the integration of thermal-mechanical coupling within a complex elastic analytical framework, and the extension of this framework to include both circular and horseshoe-shaped geometries. Furthermore, the model considers realistic boundary conditions and burial depths representative of actual mining sites, making it more applicable to engineering practice.

This study aims to develop an advanced analytical framework for analyzing the thermal-mechanical behavior of CAES chambers in abandoned coal mines. Using Cao Zhuang Coal Mine in Shandong Province as a case study, the study focuses on deriving thermal-mechanical coupling analytical solutions for both circular and horseshoe-shaped tunnels. By incorporating external loads, such as geostress and gas pressure, the study seeks to provide a comprehensive evaluation of long-term chamber stability. A comparative analysis will be conducted to assess the stability of circular and horseshoe-shaped chambers under varying thermal and mechanical conditions, identifying structural weaknesses and potential failure zones. This investigation will not only help pinpoint vulnerable areas but also provide scientific justification for selecting optimal tunnel geometries. To ensure the accuracy of the analytical solutions, finite element simulations using COMSOL 6.2 will be employed to validate theoretical models, reinforcing their applicability to real-world underground CAES designs.

This study integrates the theory of complex elasticity and derives the stress and displacement functions of a three-layer underground chamber, effectively combining thermal-mechanical effects. In Section 2, some basic equations of elasticity were reviewed. In Sections 3 and 4, the stress solution of a three-layer circular chamber was obtained by superimposing temperature stress and in-situ stress, and verified through FEM analysis. In Sections 5 and 6, the conformal transformation technique was first used to map the horseshoe shaped tunnel to a simplified computational domain, and then the analytical solution of the three-layer horseshoe shaped tunnel was calculated using the relevant knowledge of complex functions and verified by FEM analysis. Some reliable conclusions are presented in Section 7.

2. Theory of complex elasticity

The analytical solution models presented in this study are derived based on the theory of elasticity, with a particular focus on the structural behavior of three-layer circular and horseshoe-shaped chambers in abandoned mines. To ensure the validity of the analytical derivations, the following fundamental assumptions are made [12, 46]:

(1) Continuity Assumption: The material is assumed to be continuous, the deformable solid is treated as a homogeneous and densely packed continuum.

(2) Uniformity Assumption: Each layer of the studied structure is composed of a uniform material with consistent physical properties throughout.

(3) Isotropy Assumption: The material exhibits identical physical properties in all directions.

(4) Perfect Elasticity Assumption: The deformation of the material follows a linear relationship with applied stress.

(5) Small Deformation Assumption: The displacement of the structure due to external forces or temperature variations is significantly smaller than its original dimensions.

(6) Plane Strain Condition: The entire structure is considered to be in a state of plane strain, with external loads applied uniformly along the model boundaries.

According to the theory of elasticity, when an object is in a state of plane stress and subjected to a constant external force, all related problems can be formulated as boundary-value problems of the biharmonic function $U(x,\ y)$. The solution of the biharmonic function $U(x,\ y)$ requires appropriate boundary and initial conditions to be specified. Mathematically, the biharmonic function can be expressed as [47]:

$$\frac{\partial^4 U}{\partial x^4} + 2\frac{\partial^4 U}{\partial x^2 \partial y^2} + \frac{\partial^4 U}{\partial y^4} = 0. \tag{1}$$

For general and relatively simple problems in elasticity, Equation (1) can be solved with relative ease. However, for stress analyses involving complex geometric configurations or multi-connected domains, obtaining a solution in the real-number domain often becomes highly challenging. To address this issue, complex function theory can be employed as an alternative to Cartesian coordinates in Equation (1). The corresponding expression in the complex domain is given by:

$$U = \mathrm{Re}[\theta(z) + \bar{z}\varphi(z)] \tag{2}$$

where $\theta(z)$ and $\varphi(z)$ are holomorphic functions within the domain of the complex variable function. Here, $\bar{z}$ represents the complex conjugate of z, $\bar{z} = x - iy$, where i is the imaginary unit. The notation $\mathrm{Re}(\cdot)$ indicates that only the real part of the calculation result is retained.

In polar coordinates, assuming $z = re^{i\theta}$, Equation (2) can be equivalently expressed as [12]:

$$U(r,\ \theta) = \mathrm{Re}[\bar{z}\varphi(z) + \psi(z)] \tag{3}$$

where $\varphi(z)$ and $\psi(z)$ are complex functions under polar coordinate conditions.

Neglecting the influence of material strength, the stress components can be obtained by computing the second-order partial derivatives of the harmonic function $U(x,\ y)$, given by:

$$\sigma_x = \frac{\partial^2 U}{\partial y^2}, \quad \sigma_y = \frac{\partial^2 U}{\partial x^2}, \quad \tau_{xy} = -\frac{\partial^2 U}{\partial x \partial y} \tag{4}$$

where σ_x, σ_y, and τ_{xy} denote the normal stresses in the x- and y-directions and the shear stress in the xy-plane, respectively.

By substituting Equation (2) into Equation (4), the expressions for σ_x, σ_y, and τ_{xy} can be obtained:

$$\begin{cases} \sigma_x + \sigma_y = 4\,\mathrm{Re}\,[\varphi'(z)] \\ \sigma_y - \sigma_x + 2i\tau_{xy} = 2\,[\bar{z}\varphi''(z) + \psi'(z)] \\ 2G(u+iv) = \kappa\varphi(z) - z\overline{\varphi'(z)} - \psi'(z). \end{cases} \tag{5}$$

Similarly, the corresponding expressions in polar coordinates are given by:

$$\begin{cases} \sigma_\theta + \sigma_r = 2\left[\varphi'(z) + \overline{\varphi'(z)}\right] \\ \sigma_\theta - \sigma_r + 2i\tau_{r\theta} = 2e^{2i\theta}\left[\bar{z}\varphi''(z) + \psi'(z)\right] \\ 2G(u+iv) = e^{-i\theta}\left[k\varphi(z) - z\overline{\varphi'(z)} - \overline{\psi(z)}\right] \end{cases} \tag{6}$$

where G is the shear modulus, and μ is Poisson's ratio. Under plane strain conditions, the shear modulus is given by $G = E/2(1+\mu)$, and the parameter k is expressed as $k = (3-4\mu)$. The validity of Equations (5) and (6) can be mutually verified through coordinate transformation.

Since this study will later present analytical stress solutions for three-layer circular chambers and three-layer horseshoe-shaped chambers, it is necessary to map the horseshoe-shaped chamber onto the unit circle using conformal transformation during the solution process [48]. As a result, the stress representation in polar coordinates is more suitable for analyzing three-layer circular chambers. The relationship between the stress components and displacement at any given boundary point, corresponding to Equation (6), can be expressed using complex function expansion:

$$\begin{cases} \sigma_\theta + \sigma_\rho + 4\,\mathrm{Re}[\Phi(\zeta)] \\ \sigma_\theta - \sigma_\rho + 2i\tau_{\rho\theta} = \dfrac{2\zeta^2}{\rho^2\omega'(\zeta)}\left[\overline{\omega(\zeta)}\Phi'(\zeta) + \omega'(\zeta)\Psi(\zeta)\right] \\ 2G\left(u_\rho + iu_\theta\right) = \dfrac{\bar{\zeta}}{\rho}\dfrac{\overline{\omega'(\zeta)}}{|\omega(\zeta)|}\left[(3-4\mu)\varphi(\zeta) - \overline{\omega'(\zeta)\varphi'(\zeta)} - \overline{\psi(\zeta)}\right] \end{cases} \tag{7}$$

where $\Phi(\zeta) = \varphi'(\zeta)/\omega'(\zeta)$, $\Psi(\zeta) = \psi'(\zeta)/\omega'(\zeta)$, θ is the angle of any point on the ζ plane. σ_θ and σ_ρ represent circumferential and radial stress, respectively, while $\tau_{\rho\theta}$ denotes the shear stress in the radial and circumferential directions. Similarly, u_θ and u_ρ correspond to circumferential and radial displacements. The term $\omega'(\zeta)$ represents the first derivative of $\omega(\zeta)$, and $\overline{\omega'(\zeta)}$ is the conjugate function of $\omega'(\zeta)$.

For the CAES chamber model, the innermost layer of the chamber must be pressurized to maintain a stable storage environment, while the outermost layer is subjected to far-field geostress. Consequently, the boundary conditions in this model are relatively complex. For the air inside the tunnel, the boundary conditions can be formulated using complex function domain integration:

$$2G(\bar{u} + i\bar{v}) = k\varphi(t) - z\overline{\varphi'(t)} - \overline{\psi(t)} \tag{8}$$

$$\varphi(t) + z\overline{\varphi'(t)} + \overline{\psi(t)} = i\oint (X_n + iY_n)\,ds \tag{9}$$

where Equation (8) represents the displacement boundary condition, and Equation (9) corresponds to the stress boundary condition. The terms X_nX and Y_n denote the surface forces along the x- and y-axes at the circular inner boundary. The operator ds represents integration along the circular inner boundary. In Equation (9), direct integration often does not yield an analytical solution; therefore, Cauchy's integral theorem is employed for further processing.

Considering that s represents the boundary of a simply connected domain, the counterclockwise outer boundary of s is denoted as S^+, while the inner boundary is denoted as S^-. If the function $f(\zeta)$ is resolvable and $f(s)$ satisfies a boundary value problem along S^+, then:

$$\frac{1}{2\pi i}\oint \frac{f(s)}{s-\zeta}ds = f(\zeta) \quad \zeta \in S^+ \tag{10}$$

$$\frac{1}{2\pi i}\oint \frac{f(s)}{s-\zeta}ds = 0 \quad \zeta \in S^- \tag{11}$$

Similarly, if $g(\zeta)$ is resolvable on the inner boundary S^- and $g(s)$ satisfies a boundary value problem, then:

$$\frac{1}{2\pi i}\oint \frac{g(s)}{s-\zeta}ds = -g(\zeta) + g(\infty) \quad \zeta \in S^+ \tag{12}$$

$$\frac{1}{2\pi i}\oint \frac{g(s)}{s-\zeta}ds = g(\zeta) \quad \zeta \in S^-. \tag{13}$$

3. Analytical solution of a three-layer circular chamber

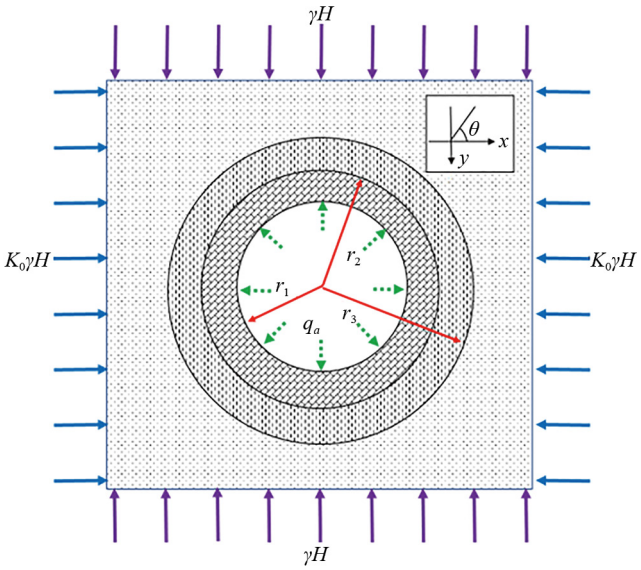

Figure 1. Schematic representation of the three-layer circular chamber

In the CAES facilities within soft rock formations, a three-layer structural design is typically employed, consisting of a sealing layer, a lining layer, and the surrounding rock [49], as illustrated in Figure 1. This figure presents the two cases analyzed in this chapter, where γ represents the bulk density of the rock, H denotes the depth from the top of the rock layer, K_0 is the lateral pressure coefficient, and q_a represents the internal load of the tunnel. The radius of the different layers

is denoted as r_1, r_2, and r_3, respectively. The external loads acting on the structure primarily include two components: geostress, which serves as an external boundary extension load, and air pressure applied at the internal boundary.

Sun et al. [12] previously derived analytical solutions for multilayer circular tunnel structures under in-situ stress and internal pressure using complex elastic mechanics. Their work verified the accuracy of such analytical approaches through comparison with FEM simulations. However, their model was limited to mechanical stresses and circular geometries. In contrast, the present study extends this analytical framework by integrating steady-state thermal effects and expanding the scope to include horseshoe-shaped chambers. These enhancements improve the model's relevance to real-world compressed air energy storage applications, where both complex geometries and thermal loads play critical roles. From Equation (3), it follows that in complex elastic mechanics, the key challenge is to derive expressions that satisfy fundamental boundary conditions while ensuring that both $\varphi(z)$ and $\psi(z)$ remain analytical functions. The analytical function for the surrounding rock in a three-layer circular tunnel structure:

Surrounding rock:

$$\begin{cases} \sigma_{r\rho} = \dfrac{\gamma H}{2}\left[(K_0+1)\left(1-\dfrac{1}{2}b_1\dfrac{r_1^2}{\rho^2}\right)+(K_0-1)\left(1-2a_1\dfrac{r_1^2}{\rho^2}-\dfrac{3}{2}b_2\dfrac{r_1^4}{\rho^4}\right)\cos 2\theta\right] \\ \sigma_{r\theta} = \dfrac{\gamma H}{2}\left[(K_0+1)\left(1+\dfrac{1}{2}b_1\dfrac{r_1^2}{\rho^2}\right)-(K_0-1)\left(1-\dfrac{3}{2}b_2\dfrac{r_1^4}{\rho^4}\right)\cos 2\theta\right] \\ \tau_{r\rho\theta} = -\dfrac{\gamma H}{2}\left[(K_0-1)\left(1+a_1\dfrac{r_1^2}{\rho^2}+\dfrac{3}{2}b_2\dfrac{r_1^4}{\rho^4}\right)\sin 2\theta\right] \\ u_{r\rho} = \dfrac{\gamma H r_1}{8G_r}\left\{(K_0+1)\,b_1\dfrac{r_1}{\rho}+(K_0-1)\left[a_1(k_r+1)\dfrac{r_1}{\rho}+b_2\dfrac{r_1^3}{\rho^3}\right]\cos 2\theta\right\} \\ v_{r\theta} = \dfrac{\gamma H r_1}{8G_r}(K_0-1)\left[-a_1(k_r-1)\dfrac{r_1}{\rho}+b_2\dfrac{r_1^3}{\rho^3}\right]\sin 2\theta \end{cases} \tag{14}$$

where a_1, b_1, and b_2 are undetermined coefficients. Similarly, the analytical functions corresponding to the sealing layer are expressed as:

$$\begin{cases} \sigma_{l\rho} = \dfrac{\gamma H}{2}\left[(K_0+1)\left(a_2'-\dfrac{1}{2}b_2'\dfrac{r_2^2}{\rho^2}\right)+(K_0-1)\left(\dfrac{1}{2}b_1'-2a_3'\dfrac{r_2^2}{\rho^2}-\dfrac{3}{2}b_3'\dfrac{r_2^4}{\rho^4}\right)\cos 2\theta\right] \\ \sigma_{l\theta} = \dfrac{\gamma H}{2}\left[(K_0+1)\left(a_2'+\dfrac{1}{2}b_2'\dfrac{r_2^2}{\rho^2}\right)+(K_0-1)\left(\dfrac{1}{2}b_1'-6a_1'\dfrac{r_2^2}{\rho^2}-\dfrac{3}{2}b_3'\dfrac{r_2^4}{\rho^4}\right)\cos 2\theta\right] \\ \tau_{l\rho\theta} = \dfrac{\gamma H}{2}\left[(K_0-1)\left(3a_1'\dfrac{\rho^2}{r_2^2}-\dfrac{1}{2}b_1'-a_3'\dfrac{r_2^2}{\rho^2}-\dfrac{3}{2}b_3'\dfrac{r_2^4}{\rho^4}\right)\sin 2\theta\right] \\ u_{lr} = \dfrac{\gamma H r_2}{8G_l}\left\{\begin{array}{l}(K_0+1)\left[a_2'(k_l-1)\dfrac{\rho}{r_2}+b_2'\dfrac{r_2}{\rho}\right] \\ +(K_0-1)\left[a_1'(k_l-3)\dfrac{\rho^3}{r_2^3}+b_1'\dfrac{\rho}{r_2}+a_3'(k_l+1)\dfrac{r_2}{\rho}+b_3'\dfrac{r_2^3}{\rho^3}\right]\cos 2\theta\end{array}\right\} \\ v_{l\theta} = \dfrac{\gamma H r_2}{8G_l}(K_0-1)\left[a_1'(k_l+3)\dfrac{\rho^3}{r_2^3}-b_1'\dfrac{\rho}{r_2}-a_3'(k_l-1)\dfrac{r_2}{\rho}+b_3'\dfrac{r_2^3}{\rho^3}\right]\sin 2\theta \end{cases} \tag{15}$$

where a_1', a_2', a_3', b_1', b_2' and b_3' are undetermined coefficients. For the lining layer, the analytical function is given by:

$$\begin{cases} \sigma_{g\rho} = \dfrac{\gamma H}{2}\left[(K_0+1)\left(c_2' - \dfrac{1}{2}d_2'\dfrac{r_3^2}{\rho^2}\right) + (K_0-1)\left(\dfrac{1}{2}d_1' - 2c_3'\dfrac{r_3^2}{\rho^2} - \dfrac{3}{2}d_3'\dfrac{r_3^4}{\rho^4}\right)\cos 2\theta\right] \\ \sigma_{g\theta} = \dfrac{\gamma H}{2}\left[(K_0+1)\left(c_2' + \dfrac{1}{2}d_2'\dfrac{r_3^2}{\rho^2}\right) + (K_0-1)\left(\dfrac{1}{2}d_1' - 6c_1'\dfrac{r_3^2}{\rho^2} - \dfrac{3}{2}d_3'\dfrac{r_3^4}{\rho^4}\right)\cos 2\theta\right] \\ \tau_{g\rho\theta} = \dfrac{\gamma H}{2}\left[(K_0-1)\left(3c_1'\dfrac{\rho^2}{r_3^2} - \dfrac{1}{2}d_1' - c_3'\dfrac{r_3^2}{\rho^2} - \dfrac{3}{2}d_3'\dfrac{r_3^4}{\rho^4}\right)\sin 2\theta\right] \\ u_{gr} = \dfrac{\gamma H r_3}{8G_g}\left\{\begin{array}{l} (K_0+1)\left[c_2'(k_g-1)\dfrac{\rho}{r_3} + d_2'\dfrac{r_3}{\rho}\right] \\ +(K_0-1)\left[c_1'(k_g-3)\dfrac{\rho^3}{r_3^3} + d_1'\dfrac{\rho}{r_3} + c_3'(k_g+1)\dfrac{r_3}{\rho} + d_3'\dfrac{r_3^3}{\rho^3}\right]\cos 2\theta \end{array}\right\} \\ v_{g\theta} = \dfrac{\gamma H r_3}{8G_g}(K_0-1)\left[c_1'(k_g+3)\dfrac{\rho^3}{r_3^3} - d_1'\dfrac{\rho}{r_3} - c_3'(k_g-1)\dfrac{r_3}{\rho} + d_3'\dfrac{r_3^3}{\rho^3}\right]\sin 2\theta \end{cases} \tag{16}$$

where c_1', c_2', c_3', d_1', d_2' and d_3' are undetermined coefficients.

The solutions are obtained by applying the boundary conditions of the three-layer circular chamber. According to Saint-Venant's principle [50], the self-weight of the rock mass can be approximated as a surface vertical load acting on the boundary, while the horizontal load is determined based on the lateral pressure coefficient under varying geological conditions. The governing boundary conditions for the chamber are given as follows:

As $r \to \infty$,

$$\begin{cases} \sigma_{r\rho} = \dfrac{\gamma H}{2}\left[(K_0+1) + (K_0-1)\cos 2\theta\right] \\ \sigma_{r\theta} = \dfrac{\gamma H}{2}\left[(K_0+1) - (K_0-1)\cos 2\theta\right] \\ \tau_{r\rho\theta} = \dfrac{\gamma H}{2}\left[(K_0-1)\sin 2\theta\right]. \end{cases} \tag{17}$$

At $r = r_1$,

$$\begin{cases} \sigma_{l\rho} = q_a \\ \tau_{l\rho\theta} = 0. \end{cases} \tag{18}$$

At $r = r_2$,

$$\begin{cases} \tau_{r\rho\theta} = 0 \\ \tau_{l\rho\theta} = 0 \\ \sigma_{r\rho} = \sigma_{l\rho} \\ u_{rr} = u_{lr}. \end{cases} \tag{19}$$

At $r = r_2$,

$$\begin{cases} \tau_{l\rho\theta} = 0 \\ \tau_{g\rho\theta} = 0 \\ \sigma_{l\rho} = \sigma_{g\rho} \\ u_{lr} = u_{gr}. \end{cases} \tag{20}$$

At $r = r_3$,

$$\begin{cases} \tau_{l\rho\theta} = 0 \\ \tau_{g\rho\theta} = 0 \\ \sigma_{l\rho} = \sigma_{g\rho} \\ u_{lr} = u_{gr}. \end{cases} \tag{21}$$

By substituting the boundary conditions of Equations (17) to (21) into Equations (14), (15), and (16), the unknown coefficients a_1, b_1, b_2, a_1', a_2', a_3', b_1', b_2', b_3', c_1', c_2', c_3', d_1', d_2' and d_3' can be determined. Due to the complexity of these expressions, further elaboration is omitted.

However, Equations (14), (15), and (16), account only for the external geostress and internal air pressure, while neglecting thermal effects. In CAES systems, temperature fluctuations during air injection and release introduce additional stress and displacement variations. Previous studies have shown that temperature changes in CAES facilities can also have an impact on the stability of tunnels [51]. In some cases, the charging-discharging cycle spans several months, allowing the temperature to stabilize. Therefore, this section derives the steady-state heat conduction analytical solution for a three-layer circular chamber based on thermo-elasticity. By applying the principle of superposition, the combined effects of thermal stress and mechanical stress yield the true stress state of the chamber.

Thermal stress due to temperature changes is an axisymmetric problem where deformation occurs primarily in the radial direction. The temperature distribution within the chamber depends solely on the radial position, that is $T = T(\rho)$, $u_\rho = u_\rho(\rho)$, $v_\theta = 0$, $\gamma_{\rho\theta} = 0$. We can obtain:

$$\begin{cases} \varepsilon_\rho = \dfrac{\partial u_\rho}{\partial \rho} = \dfrac{1-\mu^2}{E}\left(\sigma_\rho - \dfrac{\mu}{1-\mu}\sigma_\theta\right) + (1+\mu)\alpha\Delta T \\ \varepsilon_\theta = \dfrac{u_\rho}{\rho} = \dfrac{1-\mu^2}{E}\left(\sigma_\theta - \dfrac{\mu}{1-\mu}\sigma_\rho\right) + (1+\mu)\alpha\Delta T \\ \gamma_{\rho\theta} = 0 \end{cases} \tag{22}$$

where α is the coefficient of thermal expansion, and ΔT represents the temperature variation. The heat conduction equation is given by:

$$k\nabla^2 T + Q = \rho c \frac{\partial T}{\partial t} \tag{23}$$

where k is the thermal conductivity. In the absence of internal heat sources ($Q = 0$), and assuming a stabilized temperature distribution $\left(\dfrac{\partial T}{\partial t} = 0\right)$, the heat conduction equation simplifies to:

$$\nabla^2 T = 0 \tag{24}$$

which, in polar coordinates, becomes:

$$\left(\frac{d^2}{dr^2} + \frac{1}{r}\frac{d}{dr}\right) T = 0. \tag{25}$$

The general solution of Equation (25) is:

$$T(\rho) = A\ln\rho + B \tag{26}$$

where A and B are undetermined coefficients determined by boundary conditions. Considering that the inner boundary follows a convective heat transfer condition while the outer boundary is fixed, the heat transfer at the interface between the fluid and the structure follows Newton's cooling law:

$$q = h(T_w - T_f) \tag{27}$$

where T_w is the temperature outside the boundary, T_f is the temperature of the fluid in direct contact with the boundary. q is the heat flux density; h is the convective heat transfer coefficient between the boundary surface and the fluid.

For the stable state of the three-layer chamber, the thermal conductivity of each layer material is k_1, k_2 and k_3. The temperature values from inside to outside are T_1, T_2, and T_3, where the inner ambient temperature is known as T_n, the convective heat transfer coefficient h_n, and the outer temperature T_3. The equation of the first layer can be expressed as:

$$\begin{cases} -A_1 \dfrac{k_1}{r_1 h_n} = T_n - A_1 \ln r_1 - B_1 \\ A_1 \ln r_2 + B_1 = T_2. \end{cases} \tag{28}$$

Second layer:

$$\begin{cases} A_2 \ln r_2 + B_2 = T_2 \\ A_2 \ln r_3 + B_2 = T_3. \end{cases} \tag{29}$$

Third layer:

$$\begin{cases} A_3 \ln r_3 + B_3 = T_3 \\ A_3 \ln r_4 + B_3 = T_4. \end{cases} \tag{30}$$

Using the principle of continuous heat flow:

$$k_1 A_1 = k_2 A_2 = k_3 A_3. \tag{31}$$

Rearranging the terms leads to:

$$\begin{cases} \dfrac{T_n - T_2}{T_2 - T_3} = \beta_1 \\ \dfrac{T_2 - T_3}{T_3 - T_4} = \beta_2. \end{cases} \tag{32}$$

which can be simplified as:

$$\begin{cases} T_2 = \dfrac{T_n (\beta_2 + 1) + \beta_1 \beta_2 T_4}{1 + \beta_2 (\beta_1 + 1)} \\ T_3 = \dfrac{T_n + \beta_2 (\beta_1 + 1) T_4}{1 + \beta_2 (\beta_1 + 1)} \end{cases} \tag{33}$$

where $r_1^* = \dfrac{r_2}{r_1}$, $r_2^* = \dfrac{r_3}{r_2}$, $r_3^* = \dfrac{r_4}{r_3}$, $\beta_1 = \dfrac{k_2}{k_1} \dfrac{\ln r_1^* + \dfrac{k_1}{r_1 h_n}}{\ln r_2^*}$ and $\beta_2 = \dfrac{k_3}{k_2} \dfrac{\ln r_2^*}{\ln r_3^*}$.

The temperature distribution coefficients can then be determined as followed:

$$
\begin{cases}
A_1 = \dfrac{T_2 - T_N}{\ln r_1^* + \dfrac{k_1}{r_1 h_n}} \\
B_1 = \dfrac{\left(\dfrac{k_1}{r_1 h_n} - \ln r_1\right) T_2 + T_n \ln r_2}{\ln r_1^* + \dfrac{k_1}{r_1 h_n}} \\
A_2 = \dfrac{T_3 - T_2}{\ln r_2^*} \\
B_2 = \dfrac{T_2 \ln r_3 - T_3 \ln r_2}{\ln r_2^*} \\
A_3 = \dfrac{T_4 - T_3}{\ln r_3^*} \\
B_3 = \dfrac{T_3 \ln r_4 - T_4 \ln r_3}{\ln r_3^*}.
\end{cases} \tag{34}
$$

By substituting $T(\rho) = A\ln\rho + B$, the temperature distribution across each layer can be expressed as:

$$
\begin{cases}
T_1 = A_1 \ln\rho + B_1 \quad (r_1 \le \rho \le r_2) \\
T_2 = A_2 \ln\rho + B_2 \quad (r_2 \le \rho \le r_3) \\
T_3 = A_3 \ln\rho + B_3 \quad (r_3 \le \rho \le r_4).
\end{cases} \tag{35}
$$

The equilibrium differential equation in polar coordinates is given by:

$$
\begin{cases}
\dfrac{\partial \sigma_\rho}{\partial \rho} + \dfrac{1}{\rho}\dfrac{\partial \tau_{r\theta}}{\partial \theta} + \dfrac{\sigma_\rho - \sigma_\theta}{\rho} = 0 \\
\dfrac{1}{\rho}\dfrac{\partial \sigma_\theta}{\partial \theta} + \dfrac{\partial \tau_{\rho\theta}}{\partial \rho} + \dfrac{2\tau_{\rho\theta}}{\rho} = 0.
\end{cases} \tag{36}
$$

Geometric equation:

$$\begin{cases} \varepsilon_\rho = \dfrac{\partial u_\rho}{\partial \rho} \\ \varepsilon_\theta = \dfrac{u_\rho}{\rho} + \dfrac{1}{\rho}\dfrac{\partial v_\theta}{\partial \theta} \\ \gamma_{\rho\theta} = \dfrac{1}{\rho}\dfrac{\partial u_\rho}{\partial \theta} + \dfrac{\partial v_\theta}{\partial \rho} - \dfrac{v_\theta}{\rho}. \end{cases} \tag{37}$$

Deformation coordination equation:

$$\left(\frac{\partial^2}{\partial \rho^2} + \frac{2}{\rho}\frac{\partial}{\partial \rho}\right)\varepsilon_\theta + \left(\frac{1}{\rho^2}\frac{\partial^2}{\partial \theta^2} - \frac{1}{\rho}\frac{\partial}{\partial \rho}\right)\varepsilon_\rho = \left(\frac{1}{\rho^2}\frac{\partial^2}{\partial \theta^2} + \frac{1}{\rho}\frac{\partial^2}{\partial \rho \partial \theta}\right)\gamma_{\rho\theta}. \tag{38}$$

The temperature change function of an object is defined as $\Theta = \alpha T$, the physical equation for an axisymmetric plane strain condition under temperature variations can be formulated as:

$$\begin{cases} \sigma_\rho = \dfrac{E(1-\mu)}{(1+\mu)(1-2\mu)}\left[\varepsilon_\rho + \dfrac{\mu}{1-\mu}\varepsilon_\theta\right] - \dfrac{E}{1-2\mu}\alpha T \\ \sigma_\theta = \dfrac{E(1-\mu)}{(1+\mu)(1-2\mu)}\left[\varepsilon_\theta + \dfrac{\mu}{1-\mu}\varepsilon_\rho\right] - \dfrac{E}{1-2\mu}\alpha T \\ \tau_{\rho\theta} = \dfrac{E}{2(1+\mu)}\gamma_{\rho\theta}. \end{cases} \tag{39}$$

The strain is:

$$\begin{cases} \varepsilon_\rho = \dfrac{1-\mu^2}{E}\left[\sigma_\rho - \dfrac{\mu}{1-\mu}\sigma_\theta\right] + (1+\mu)\alpha T \\ \varepsilon_\theta = \dfrac{1-\mu^2}{E}\left[\sigma_\theta - \dfrac{\mu}{1-\mu}\sigma_\rho\right] + (1+\mu)\alpha T \\ \gamma_{\rho\theta} = \dfrac{2(1+\mu)}{E}\tau_{\rho\theta}. \end{cases} \tag{40}$$

Substituting Equation (39) into equilibrium Equation (36) yields the equilibrium equation expressed in strain:

$$\begin{cases} \dfrac{\partial \varepsilon_\rho}{\partial \rho} + \dfrac{\mu}{1-\mu}\dfrac{\partial \varepsilon_\theta}{\partial \rho} + \dfrac{1}{2}\dfrac{1-2\mu}{1-\mu}\dfrac{1}{\rho}\dfrac{\partial \gamma_{\rho\theta}}{\partial \theta} + \dfrac{1-2\mu}{1-\mu}\dfrac{\varepsilon_\rho - \varepsilon_\theta}{\rho} - \dfrac{1+\mu}{1-\mu}\alpha\dfrac{\partial T}{\partial \rho} = 0 \\ \dfrac{1}{\rho}\dfrac{\partial \varepsilon_\theta}{\partial \theta} + \dfrac{\mu}{1-\mu}\dfrac{1}{\rho}\dfrac{\partial \varepsilon_\rho}{\partial \theta} + \dfrac{1}{2}\dfrac{1-2\mu}{1-\mu}\dfrac{\partial \gamma_{\rho\theta}}{\partial \rho} + \dfrac{1-2\mu}{1-\mu}\dfrac{\gamma_{\rho\theta}}{\rho} - \dfrac{1+\mu}{1-\mu}\alpha\dfrac{1}{\rho}\dfrac{\partial T}{\partial \theta} = 0. \end{cases} \tag{41}$$

Assuming the existence of a displacement potential function Φ, the specific solution to the displacement equilibrium equation can be expressed as:

$$\begin{cases} u_\rho = \dfrac{\partial \Psi(\rho,\ \theta)}{\partial \rho} \\ \\ v_\theta = \dfrac{1}{\rho}\dfrac{\partial \Psi(\rho,\ \theta)}{\partial \theta}. \end{cases} \tag{42}$$

By substituting Equations (37) and (41) into Equation (40), we obtain:

$$\begin{cases} \dfrac{\partial}{\partial \rho}\left(\nabla^2 \Psi\right) - (1+\mu)^2 \alpha \dfrac{\partial T}{\partial r} = 0 \\ \\ \dfrac{1}{\rho}\dfrac{\partial}{\partial \theta}\left(\nabla^2 \Psi\right) - (1+\mu)^2 \alpha \dfrac{1}{\rho}\dfrac{\partial T}{\partial \theta} = 0. \end{cases} \tag{43}$$

where $\nabla^2 = \dfrac{\partial^2}{\partial \rho^2} + \dfrac{1}{\rho}\dfrac{\partial}{\partial \rho} + \dfrac{1}{\rho^2}\dfrac{\partial^2}{\partial \theta^2}$. When Equation (42) holds, it can be further expressed as:

$$\nabla^2 \Psi = \frac{1+\mu}{1-\mu}\alpha T. \tag{44}$$

The general expression for stress in this system is given by:

$$\begin{cases} \sigma_\rho = -\dfrac{E}{(1-\mu)(1+\mu)^2}\left(\dfrac{1}{\rho}\dfrac{\partial \Psi}{\partial \rho} + \dfrac{1}{\rho^2}\dfrac{\partial^2 \Psi}{\partial \theta^2}\right) \\ \\ \sigma_\theta = -\dfrac{E}{(1-\mu)(1+\mu)^2}\dfrac{\partial^2 \Psi}{\partial \rho^2} \\ \\ \tau_{\rho\theta} = \dfrac{E}{(1-\mu)(1+\mu)^2}\dfrac{\partial}{\partial \rho}\left(\dfrac{1}{\rho}\dfrac{\partial \Psi}{\partial \theta}\right). \end{cases} \tag{45}$$

For axisymmetric problems, the following relationships hold:

$$T = T(\rho), \quad \Psi = \Psi(\rho). \tag{46}$$

The corresponding displacement characteristic solution is given as:

$$\begin{cases} u_\rho = \dfrac{d\Psi(\rho)}{d\rho} \\ \\ v_\theta = 0. \end{cases} \tag{47}$$

By integrating Equation (50) twice, it can be rewritten as:

$$\Psi(\rho)=\frac{1+\mu}{1-\mu}\alpha\int\frac{1}{\rho}\left(\int\rho T(\rho)d\rho\right)d\rho+\frac{1+\mu}{1-\mu}\alpha C_1\ln\rho+C_2 \tag{48}$$

where C_1 and C_2 are constant coefficients. By substituting formula (47) into formula (44):

$$\begin{cases}\sigma_\rho^I=-\dfrac{E\alpha}{1-\mu^2}\dfrac{1}{\rho^2}\left[\int\rho T(\rho)d\rho+C_1\right]\\ \sigma_\theta^I=\dfrac{E\alpha}{1-\mu^2}\dfrac{1}{\rho^2}\left[\int\rho T(\rho)d\rho+C_1-\rho^2T(\rho)\right]\\ \tau_{\rho\theta}^I=0.\end{cases} \tag{49}$$

Equation (48) represents only a particular solution to the equilibrium Equation (36); thus, an additional supplementary solution must be introduced to account for thermal stress effects. Considering the axisymmetric nature of the problem and the uniform boundary force distribution, a stress function satisfying the compatibility equation is chosen:

$$\Phi(\rho)=\frac{C_3}{2}\rho^2 \tag{50}$$

where C_3 is a constant coefficient, and the corresponding stress component can be expressed as:

$$\begin{cases}\sigma_\rho^{II}=\dfrac{1}{\rho}\dfrac{\partial\Phi(\rho)}{\partial\rho}+\dfrac{1}{\rho^2}\dfrac{\partial^2\Phi(\rho)}{\partial\theta^2}=C_3\\ \sigma_\theta^{II}=\dfrac{\partial^2\Phi(\rho)}{\partial\rho^2}=C_3\\ \tau_{\rho\theta}^{II}=-\dfrac{\partial}{\partial\rho}\left(\dfrac{1}{\rho}\dfrac{\partial\Phi(\rho)}{\partial\rho}\right)=0.\end{cases} \tag{51}$$

By superimposing the solutions from Equations (48) and (50), the total stress in the axisymmetric model is obtained as:

$$\begin{cases}\sigma_r^T=\sigma_r^I+\sigma_r^{II}=-\dfrac{E\alpha}{1-\mu^2}\dfrac{1}{\rho^2}\left[\int\rho T(\rho)d\rho+C_1\right]+C_3\\ \sigma_\theta^T=\sigma_\theta^I+\sigma_\theta^{II}=\dfrac{E\alpha}{1-\mu^2}\dfrac{1}{\rho^2}\left[\int\rho T(\rho)d\rho+C_1-\rho^2T(\rho)\right]+C_3\\ \tau_{\rho\theta}^T=\tau_{\rho\theta}^I+\tau_{\rho\theta}^{II}=0.\end{cases} \tag{52}$$

For the integral solution $\int\rho T(\rho)d\rho$, the following conditions hold:

$$\begin{aligned}\int_{\rho_i}^{\rho}\rho T(\rho)d\rho &= \int_{\rho_i}^{\rho}\rho(A\ln\rho+B)d\rho = A\int_{\rho_i}^{\rho}\rho\ln\rho d\rho + B\int_{\rho_i}^{\rho}\rho d\rho \\ &= A\left(\frac{\rho^2\ln\rho}{2}-\frac{\rho^2}{4}\right)_{\rho_i}^{\rho}+B\left(\frac{\rho^2}{2}\right)_{\rho_i}^{\rho}.\end{aligned} \tag{53}$$

At this stage, the thermal stress and displacement expressions for different layers of the chamber can be formulated as follows:

Sealing layer (first layer):

$$\begin{cases}\sigma_{1\rho}^{T} = -\dfrac{E_1\alpha_1}{1-\mu_1^2}\dfrac{1}{\rho^2}\left[A_1\left(\dfrac{\rho^2\ln\rho}{2}-\dfrac{\rho^2}{4}\right)_{\rho_1}^{\rho}+B_1\left(\dfrac{\rho^2}{2}\right)_{\rho_1}^{\rho}+C_{11}\right]+C_{13} \\ \sigma_{1\theta}^{T} = \dfrac{E_1\alpha_1}{1-\mu_1^2}\dfrac{1}{\rho^2}\left[A_1\left(\dfrac{\rho^2\ln\rho}{2}-\dfrac{\rho^2}{4}\right)_{\rho_1}^{\rho}+B_1\left(\dfrac{\rho^2}{2}\right)_{\rho_1}^{\rho}+C_{11}-\rho^2\left(A_1\ln\rho+B_1\right)\right]+C_{13} \\ u_{1r}^{T} = \dfrac{1+\mu_1}{1-\mu_1}\alpha_1\left[A_1\left(\dfrac{\rho^2\ln\rho}{2}-\dfrac{\rho^2}{4}\right)_{\rho_1}^{\rho}+B_1\left(\dfrac{\rho^2}{2}\right)_{\rho_1}^{\rho}\right]+\dfrac{1+\mu_1}{1-\mu_1}\alpha_1 C_{11}.\end{cases} \tag{54}$$

Lining layer (second layer):

$$\begin{cases}\sigma_{2r}^{T} = -\dfrac{E_2\alpha_2}{1-\mu_2^2}\dfrac{1}{\rho^2}\left[A_2\left(\dfrac{\rho^2\ln\rho}{2}-\dfrac{\rho^2}{4}\right)_{\rho_2}^{\rho}+B_2\left(\dfrac{\rho^2}{2}\right)_{\rho_2}^{\rho}+C_{21}\right]+C_{23} \\ \sigma_{2\theta}^{T} = \dfrac{E_2\alpha_2}{1-\mu_2^2}\dfrac{1}{\rho^2}\left[A_2\left(\dfrac{\rho^2\ln\rho}{2}-\dfrac{\rho^2}{4}\right)_{\rho_2}^{\rho}+B_2\left(\dfrac{\rho^2}{2}\right)_{\rho_2}^{\rho}+C_{21}-\rho^2\left(A_2\ln\rho+B_2\right)\right]+C_{23} \\ u_{2r}^{T} = \dfrac{1+\mu_2}{1-\mu_2}\alpha_2\left[A_2\left(\dfrac{\rho^2\ln\rho}{2}-\dfrac{\rho^2}{4}\right)_{\rho_2}^{\rho}+B_2\left(\dfrac{\rho^2}{2}\right)_{\rho_2}^{\rho}\right]+\dfrac{1+\mu_2}{1-\mu_2}\alpha_2 C_{21}.\end{cases} \tag{55}$$

Surrounding rock layer (third layer):

$$\begin{cases}\sigma_{3\rho}^{T} = -\dfrac{E_3\alpha_3}{1-\mu_3^2}\dfrac{1}{\rho^2}\left[A_3\left(\dfrac{\rho^2\ln\rho}{2}-\dfrac{\rho^2}{4}\right)_{\rho_3}^{\rho}+B_3\left(\dfrac{\rho^2}{2}\right)_{\rho_3}^{\rho}+C_{31}\right]+C_{33} \\ \sigma_{3\theta}^{T} = \dfrac{E_3\alpha_3}{1-\mu_3^2}\dfrac{1}{\rho^2}\left[A_3\left(\dfrac{\rho^2\ln\rho}{2}-\dfrac{\rho^2}{4}\right)_{\rho_3}^{\rho}+B_3\left(\dfrac{\rho^2}{2}\right)_{\rho_3}^{\rho}+C_{31}-\rho^2\left(A_3\ln\rho+B_3\right)\right]+C_{33} \\ u_{3\rho}^{T} = \dfrac{1+\mu_3}{1-\mu_3}\alpha_3\left[A_3\left(\dfrac{\rho^2\ln\rho}{2}-\dfrac{\rho^2}{4}\right)_{\rho_3}^{\rho}+B_3\left(\dfrac{\rho^2}{2}\right)_{\rho_3}^{\rho}\right]+\dfrac{1+\mu_3}{1-\mu_3}\alpha_3 C_{31}.\end{cases} \tag{56}$$

The coefficients $C_{11}, C_{13}, C_{21}, C_{23}, C_{31}$ and C_{33} are determined by solving the boundary conditions:

$$\begin{cases} r \to r_1: & \sigma_{1\rho}^T = 0 \\ r \to r_2: & \sigma_{1\rho}^T = \sigma_{2\rho}^T; \quad u_{1\rho}^T = u_{2\rho}^T \\ r \to r_3: & \sigma_{2\rho}^T = \sigma_{3\rho}^T; \quad u_{2\rho}^T = u_{3\rho}^T \\ r \to r_4: & \sigma_{3\rho}^T = 0. \end{cases} \tag{57}$$

The expanded form of Equation (57) is:

$$\begin{cases} -\dfrac{E_1\alpha_1}{1-\mu_1^2}\dfrac{1}{\rho_1^2}C_{11} + C_{13} = 0 \\ -\dfrac{E_1\alpha_1}{1-\mu_1^2}\dfrac{1}{\rho_2^2}\left[A_1\left(\dfrac{\rho^2\ln\rho}{2} - \dfrac{\rho^2}{4}\right)_{\rho_1}^{\rho_2} + B_1\left(\dfrac{\rho^2}{2}\right)_{\rho_1}^{\rho_2} + C_{11}\right] + C_{13} = -\dfrac{E_2\alpha_2}{1-\mu_2^2}\dfrac{1}{\rho_2^2}C_{21} + C_{23} \\ \dfrac{1+\mu_1}{1-\mu_1}\alpha_1\left[A_1\left(\dfrac{\rho^2\ln\rho}{2} - \dfrac{\rho^2}{4}\right)_{\rho_1}^{\rho_2} + B_1\left(\dfrac{\rho^2}{2}\right)_{\rho_1}^{\rho_2}\right] + \dfrac{1+\mu_1}{1-\mu_1}\alpha_1 C_{11} = \dfrac{1+\mu_2}{1-\mu_2}\alpha_2 C_{21} \\ -\dfrac{E_2\alpha_2}{1-\mu_2^2}\dfrac{1}{\rho_3^2}\left[A_2\left(\dfrac{\rho^2\ln\rho}{2} - \dfrac{\rho^2}{4}\right)_{\rho_2}^{\rho_3} + B_2\left(\dfrac{\rho^2}{2}\right)_{\rho_2}^{\rho_3} + C_{21}\right] + C_{23} = -\dfrac{E_3\alpha_3}{1-\mu_3^2}\dfrac{1}{\rho_3^2}C_{31} + C_{33} \\ \dfrac{1+\mu_2}{1-\mu_2}\alpha_2\left[A_2\left(\dfrac{\rho^2\ln\rho}{2} - \dfrac{\rho^2}{4}\right)_{\rho_2}^{\rho_3} + B_2\left(\dfrac{\rho^2}{2}\right)_{\rho_2}^{\rho_3}\right] + \dfrac{1+\mu_2}{1-\mu_2}\alpha_2 C_{21} = \dfrac{1+\mu_3}{1-\mu_3}\alpha_3 C_{31} \\ -\dfrac{E_3\alpha_3}{1-\mu_3^2}\dfrac{1}{\rho_4^2}\left[A_3\left(\dfrac{\rho^2\ln\rho}{2} - \dfrac{\rho^2}{4}\right)_{\rho_3}^{\rho_4} + B_3\left(\dfrac{\rho^2}{2}\right)_{\rho_3}^{\rho_4} + C_{31}\right] + C_{33} = 0. \end{cases} \tag{58}$$

Definition, $\lambda_i = \dfrac{E_i\alpha_i}{1-\mu_i^2}$, $\eta_i = \dfrac{1+\mu_i}{1-\mu_i}\alpha_i$, $\xi_i = A_i\left(\dfrac{\rho^2\ln\rho}{2} - \dfrac{\rho^2}{4}\right)_{\rho_i}^{\rho_{i+1}} + B_i\left(\dfrac{\rho^2}{2}\right)_{\rho_i}^{\rho_{i+1}}$, $i = 1,\ 2,\ 3$. The augmented matrix composed of the boundary conditions is expressed as:

$$\begin{bmatrix} -\lambda_1\frac{1}{r_1^2}C_{11} & +C_{13} & & & & & = 0 \\ -\lambda_1\frac{1}{r_2^2}C_{11} & +C_{13} & +\lambda_2\frac{1}{r_2^2}C_{21} & -C_{23} & & & = \lambda_1\frac{1}{r_2^2}\xi_1 \\ \eta_1 C_{11} & & -\eta_2 C_{21} & & & & -\eta_1\xi_1 \\ & & -\lambda_2\frac{1}{r_3^2}C_{21} & +C_{23} & +\lambda_3\frac{1}{r_3^2}C_{31} & -C_{33} & = \lambda_2\frac{1}{r_3^2}\xi_2 \\ & & \eta_2 C_{21} & & -\eta_3 C_{31} & & = -\eta_2\xi_2 \\ & & & & -\lambda_3\frac{1}{r_4^2}C_{31} & +C_{33} & = \lambda_3\frac{1}{r_4^2}\xi_3 \end{bmatrix}. \tag{59}$$

Using Cramer's Rule to solve the system of Equations (59), the unknown coefficients can be determined as:

$$C_{11} = \frac{D_1}{D},\ C_{13} = \frac{D_2}{D},\ C_{21} = \frac{D_3}{D},\ C_{23} = \frac{D_4}{D},\ C_{31} = \frac{D_5}{D},\ C_{33} = \frac{D_6}{D}. \tag{60}$$

The solutions to Equation (60) provide the numerical values for the unknown coefficients $C_{11}, C_{13}, C_{21}, C_{23}, C_{31}$ and C_{33}. To illustrate the derivation process, Figure 2 presents a flowchart summarizing the computational steps.

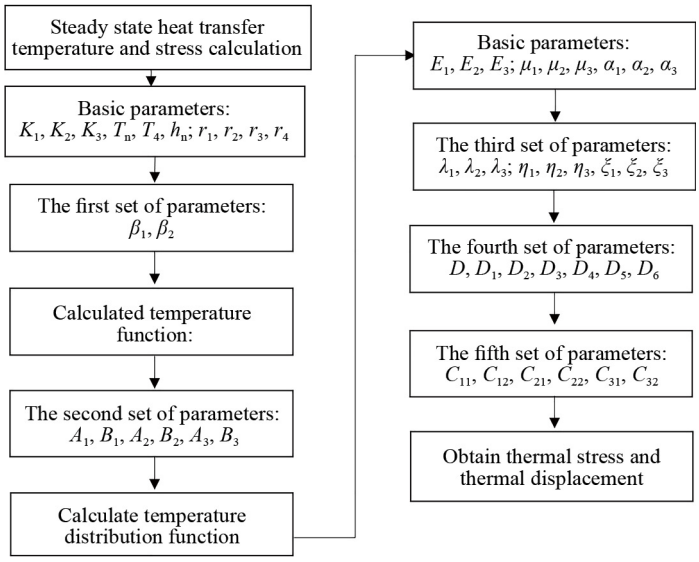

Figure 2. Flowchart of the formula derivation process

Through the derivation above, the stress and displacement expressions for each layer of the chamber have been obtained. The final expression for the total stress, accounting for external geostress, internal air pressure, and thermal effects, is given by:

$$\begin{cases} \sigma_\rho = \sigma_{i\rho} + \sigma_r^I + \sigma_r^{II} \\ \sigma_\theta = \sigma_{i\theta} + \sigma_\theta^I + \sigma_\theta^{II} \\ \tau_{\rho\theta} = \tau_{i\rho\theta} \\ u_\rho = u_{i\rho} + u_\rho^I + u_\rho^{II} \\ v_\theta = v_{i\theta}. \end{cases} \tag{61}$$

4. Verification of the three-layer circular chamber

In the previous section, the thermo-mechanical coupling analytical solution for a three-layer circular tunnel under steady-state conditions was derived. To validate the accuracy of the derived results, this section compares them with FEM simulations conducted using COMSOL 6.2, which 6.2 was selected as the FEM platform for simulating our model due to its powerful capabilities in handling coupled physics problems, particularly those involving structural mechanics and heat transfer. The comparison is presented through line graphs and contour plots. The material parameters used in the calculations are provided in Table 2.

Table 2. Material parameters used in the calculation

	Sealing layer	Lining layer	Surrounding rock layer
E (GPa)	210	30	13.5
v	0.20	0.27	0.25
ρ (kg/m^3)	7,800	2,500	1,800
α (1/K)	1.7×10^{-5}	1.2×10^{-5}	1.2×10^{-5}
K (W/m · K)	45	1.4	3.5
c_ρ (J/kg · K)	500	837	1,000

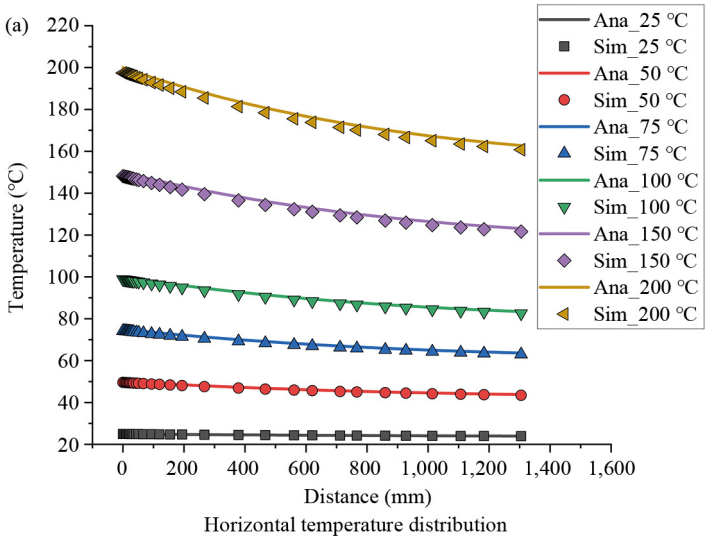

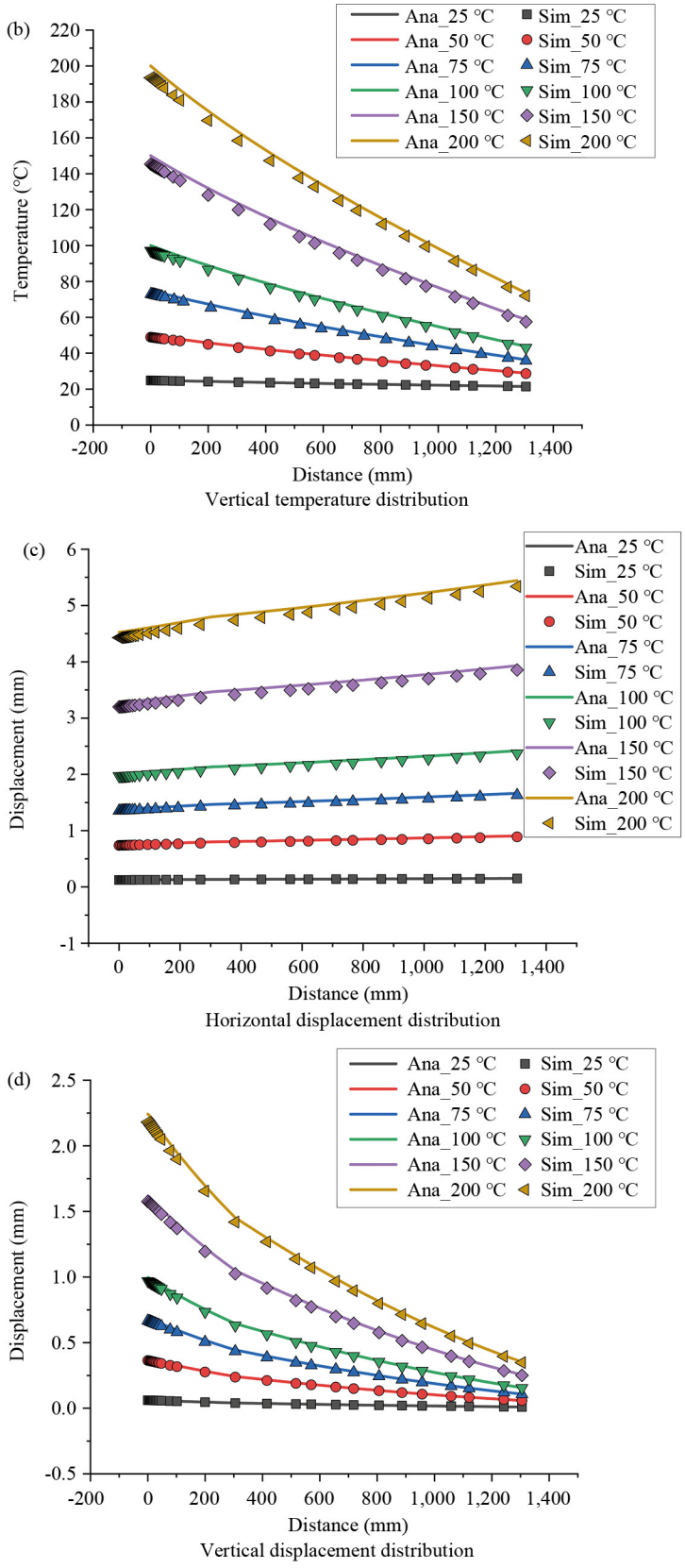

Figure 3. Comparison of line graphs with finite element calculation results

Figure 3 presents a comparison between the analytical and numerical solutions for the tunnel's horizontal and vertical directions under different temperature conditions. The selected temperatures for analysis include 25 °C, 50 °C, 75 °C, 100 °C, 150 °C, and 200 °C. We calculated the relative error of the line graph, as shown in Table 3, and the results clearly indicate that the thermal coupling analysis solution obtained in this study is very consistent with the FEM results, thus verifying the accuracy of the analysis method.

Table 3. Relative error analysis of analytical solutions and fem results for circular chambers

Temperature	Horizontal temperature error (%)	Vertical temperature error (%)	Horizontal temperature error (%)	Vertical temperature error (%)
25 °C	0.273	0.564	1.567	1.749
50 °C	0.842	1.863	2.103	2.542
75 °C	1.041	2.703	2.201	4.352
100 °C	1.139	2.615	2.710	4.252
150 °C	1.241	2.883	3.168	3.938
200 °C	1.292	3.021	2.495	4.559

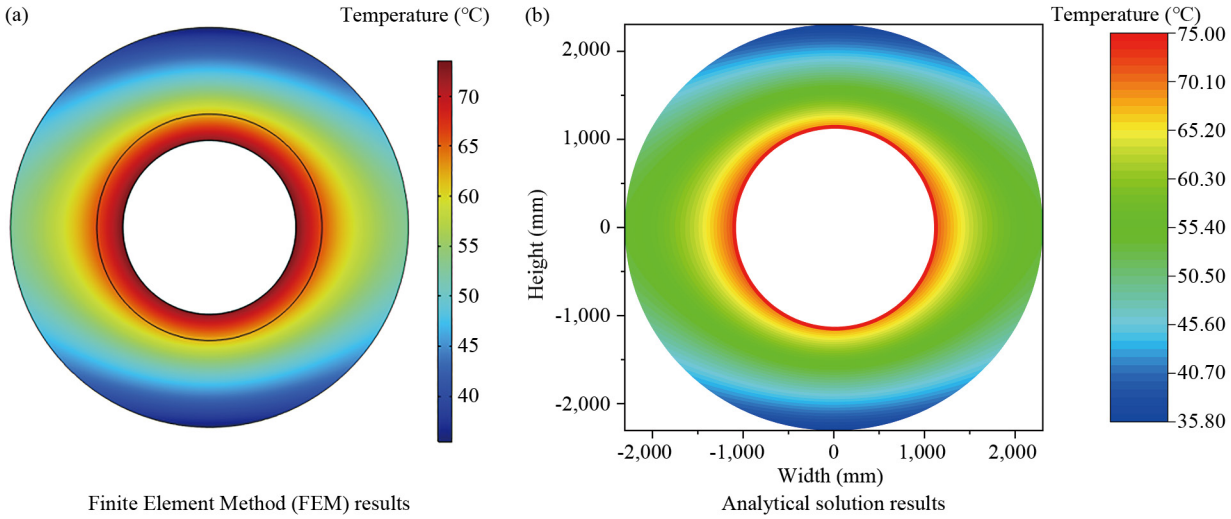

Figure 4. Comparison of temperature distributions in the chamber at 75 °C

While Figure 3 provides a comparative analysis of the two extreme directions (horizontal and vertical), it does not capture the overall distribution or localized stress variations under general conditions. To further assess the applicability of the analytical solution, this study examines the first principal stress (σ_1) contour maps of the tunnel at different burial depths (100 m, 140 m, 180 m, 200 m, and 400 m) under a temperature of 75 °C, a lateral pressure coefficient of 1.5, and a tunnel pressure of 8 MPa. The results are presented in Figure 4, where (a) and (b) illustrate the temperature distribution obtained from FEM and the analytical solution, respectively. The comparison confirms that the temperature distributions in both approaches are highly consistent. A more detailed analysis of the temperature fields reveals distinct thermal behaviors across the three layers of the chamber. The sealing layer (innermost) experiences the sharpest temperature gradient, as it is in direct contact with the compressed air and therefore absorbs heat rapidly. This indicates its lower thermal inertia and critical role in resisting rapid thermal expansion. The lining layer serves as a transitional zone, where temperature changes are more gradual, helping to buffer thermal stress between the hot interior and the relatively stable surrounding rock. The outermost rock layer exhibits minimal temperature variation due to its large thermal mass and

insulating characteristics, confirming its role as a natural thermal barrier. These differences highlight the importance of layer-specific thermal management in underground energy storage system designs.

Furthermore, Figure 5 compare the first principal stress contour maps at different burial depths. The comparison reveals that there is only a slight discrepancy between the two results in the sealing layer. The FEM results provide better resolution in characterizing localized stress variations, while the analytical solution indicates that the entire sealing layer experiences high stress levels. Nevertheless, the numerical values derived from both methods exhibit strong agreement, indicating that the analytical solution remains applicable under general conditions and is sufficiently accurate for addressing localized stress distributions.

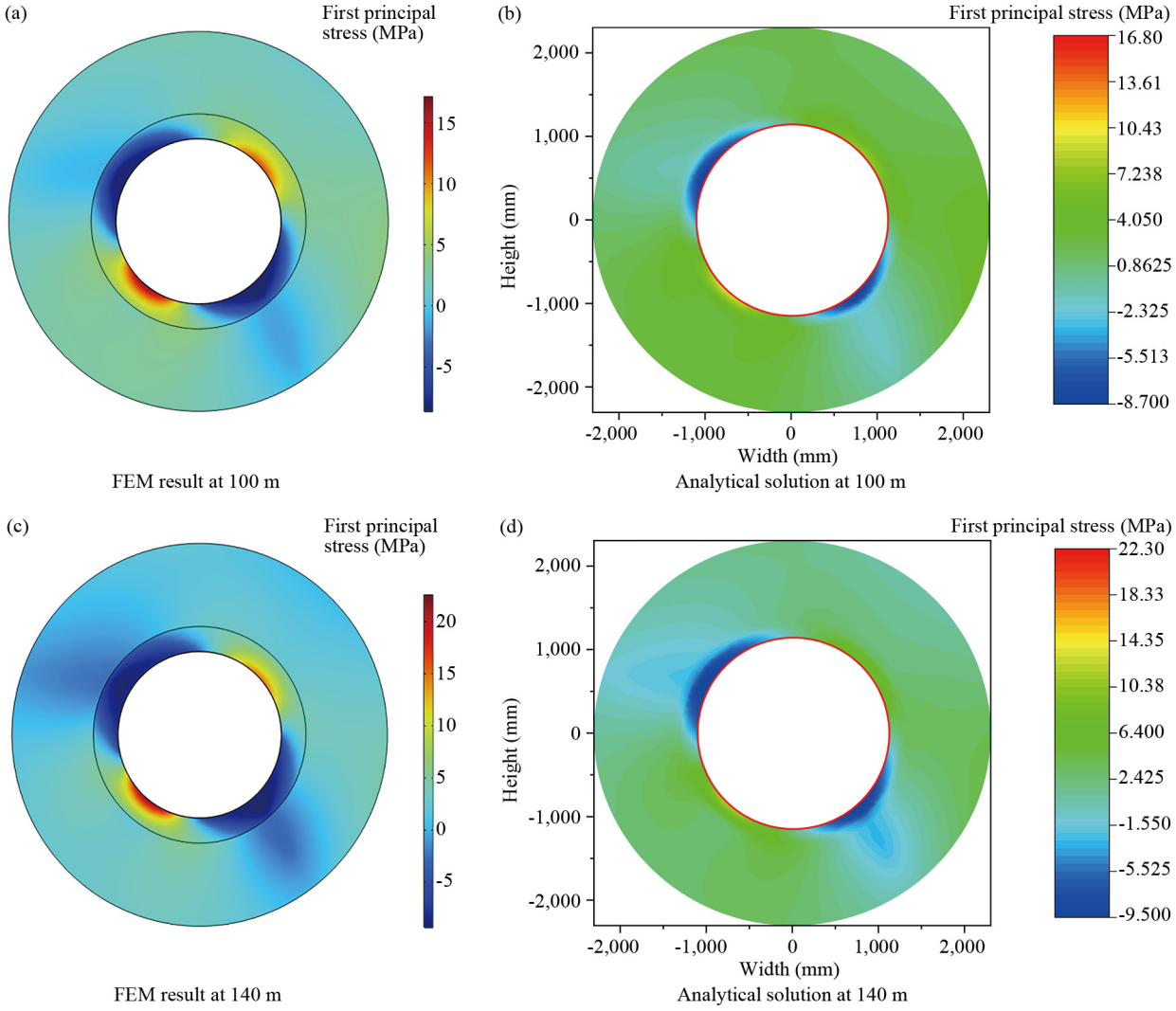

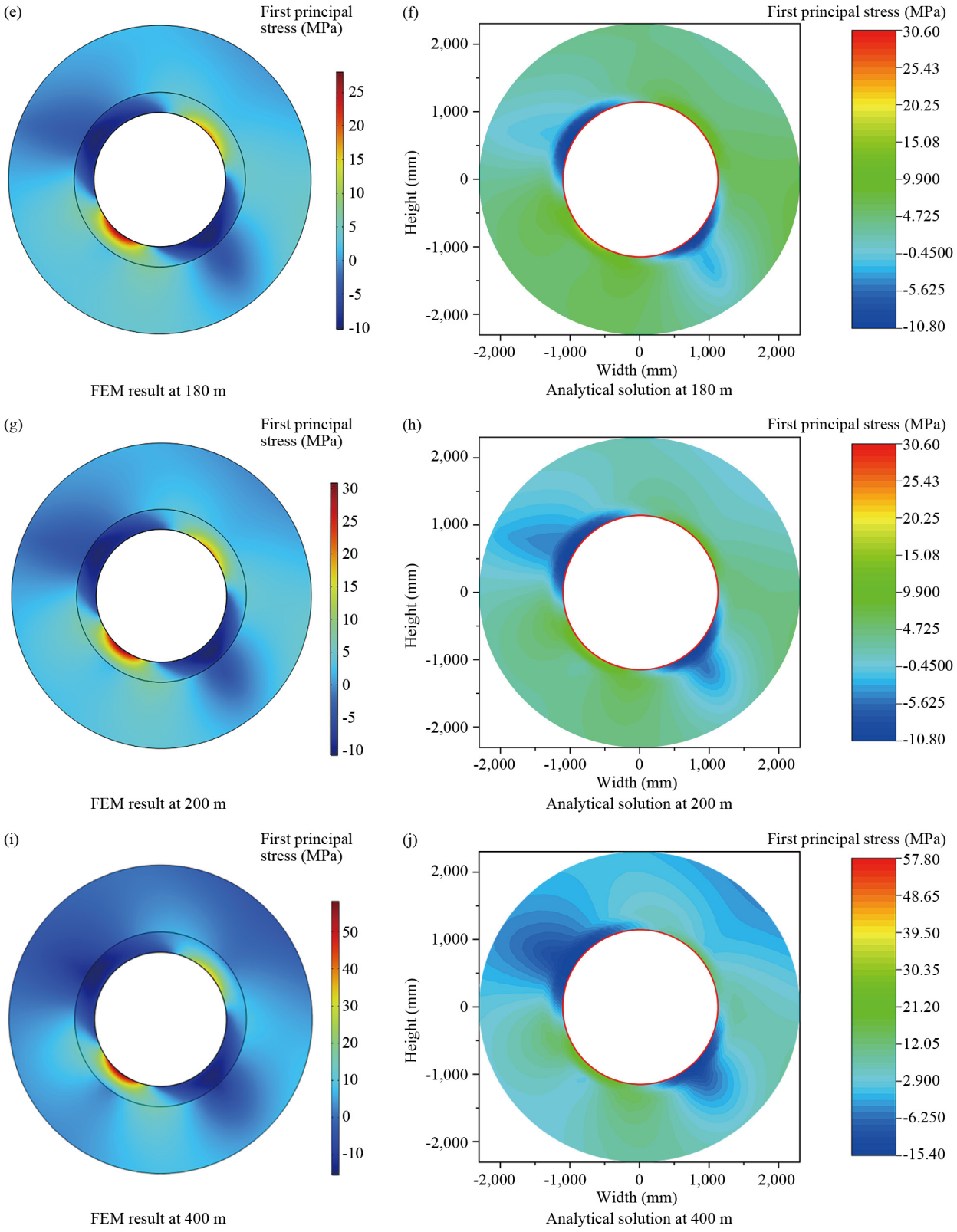

Figure 5. Comparison of first principal stress contour maps at different burial depths

The comparative analysis demonstrates that the analytical solution derived in this study is not only effective in predicting stress distributions within the three-layer circular chamber but also provides results that are highly consistent with those obtained through finite element simulations. This further establishes the reliability and accuracy of the proposed analytical approach for thermo-mechanical coupling analysis.

5. Analytical solution for a three-layer horseshoe-shaped chamber

For horseshoe-shaped chambers, describing their geometry using elementary functions in Cartesian coordinates is inherently complex. Therefore, when addressing such problems, conformal transformations are typically employed. These transformations allow for the calculation of the corresponding mapping functions in a transformed domain, facilitating the derivation of analytical solutions based on complex elastic mechanics [52]. In the field of complex function theory, solving for stress and displacement in tunnel structures generally involves three key steps:

(1) Conformal Transformation and Mapping Function Computation

The shape of the tunnel is mapped from the Z plane to the ζ plane, where the tunnel's irregular shape is transformed into a regular domain. The mapping function for this transformation is expressed as:

$$z = \omega(\zeta) = R\left(\zeta + \sum_{N=0}^{\infty} C_N \zeta^{-N}\right) \tag{62}$$

where R is a constant in the real number field, generally representing the radius size of the tunnel, and C_N is a constant in the complex number field. The number of N affects the accuracy of the tunnel shape mapping. Generally, the more N there are, the higher the accuracy.

(2) Establishing the Complex Stress Function

Based on the stress and displacement boundary conditions of the tunnel's environment, an appropriate complex stress function is determined. In this study, the power series method is employed to derive two complex stress functions.

(3) Solving for Stress and Displacement

The obtained stress functions are then used to derive analytical expressions for stress and displacement at any given point in the three-layer horseshoe-shaped chamber.

In underground coal mines, tunnel cross-sections are often highly irregular. Conformal transformation provides an effective method for mapping these complex geometries into a computationally manageable form. The transformation is used to map the Z plane (physical domain) onto the ζ plane (a unit circle in the complex plane), as illustrated in Figure 6.

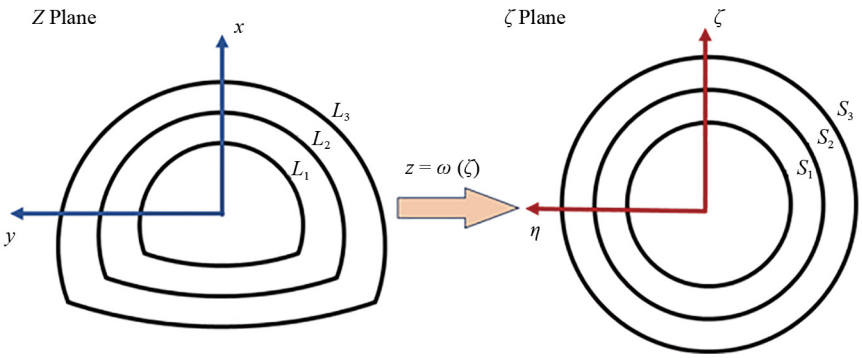

Figure 6. Theoretical representation of conformal transformation

The horseshoe-shaped tunnel considered in this study follows a conventional two-lane arched roadway design, with dimensions provided in Figure 6. To optimize the accuracy of the conformal transformation, multiple values of N were tested, and the mapping function terms were analyzed accordingly. The corresponding coefficients for different values of N are presented in Table 4, while the mapped tunnel shapes are also shown in Figure 7. Based on comparative analysis, it was found that when $N = 8$, the mapped tunnel shape closely matches the actual tunnel geometry, with a negligible error of only 0.049%.

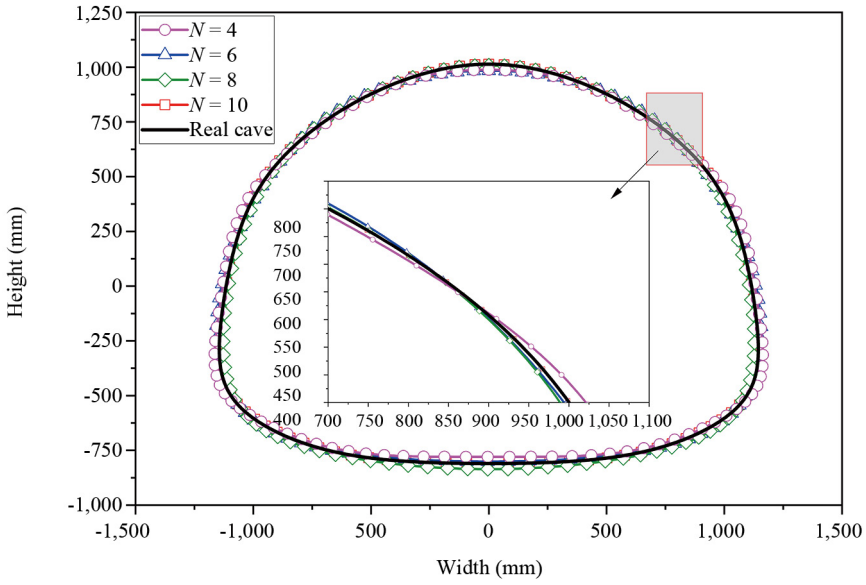

Figure 7. Actual tunnel cross-section and comparison of tunnel shapes generated by different mapping functions

Table 4. Coefficients for conformal transformation with different values of N

Parameter	$N = 4$	$N = 6$	$N = 8$	$N = 10$
C0	0.0155	0.01	0.02	0.018
C1	−0.12	−0.1	−0.13	−0.11
C2	0.0718	0.07	0.075	0.073
C3	−0.0298	−0.03	−0.028	−0.027
C4		0.002	0.0025	0.0023
C5		0.008	0.009	0.0085
C6			0.0017	0.0031
C7			−0.0093	−0.0034
C8				0.0006
C9				0.0004

As introduced in Section 3.1, the construction of CAES projects in horseshoe shaped chambers still requires a three-layer structure, as shown in Figure 8. From the inside out are the sealing layer L_1, lining layer L_2, and surrounding rock layer L_3. The innermost side of the tunnel receives a uniformly distributed load of gas pressure q, while the outermost side is affected by geostress. The load on the topmost side is γH, and on the lateral side is $K_0 \gamma H$, where K_0 is the lateral pressure coefficient. It should be pointed out that the boundaries of each layer need to satisfy the boundary continuity condition, and for this irregular horseshoe shaped tunnel calculation, the most convenient method currently is to use

conformal transformation to calculate on the Zeta plane. The sealing layer L_1 after conformal transformation corresponds to the mapping area S_1, the lining layer L_2 corresponds to the mapping area S_2, and the mapping area corresponding to the surrounding rock layer L_3 is assumed to be S_3. For the load characteristics in the S_3 region, the load stress function can be expressed as:

$$\begin{cases} \varphi_1(\zeta) = \Gamma\omega(\zeta) + \varphi_0(\zeta) \\ \psi_1(\zeta) = \Gamma'\omega(\zeta) + \psi_0(\zeta) \end{cases} \tag{63}$$

where

$$\begin{cases} \varphi_0(\zeta) = \sum_{k=0}^{\infty} h_k \zeta^{-k} \\ \psi_0(\zeta) = \sum_{k=0}^{\infty} m_k \zeta^{-k} \end{cases} \tag{64}$$

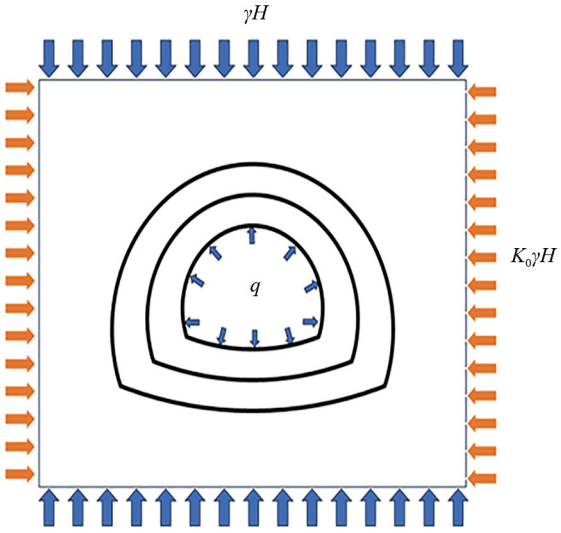

Figure 8. Schematic representation of a three-layer horseshoe-shaped chamber

Using the Saint-Venant principle, Lu et al. [53, 54] proposed a method for solving the far-field stress boundary condition, which can be written as:

$$\begin{cases} \Gamma = \dfrac{1+K}{4}\gamma H \\ \Gamma' = -(1-K)\gamma H \end{cases} \tag{65}$$

For the stress function in the S_2 region, a polynomial representation is required:

$$\begin{cases} \varphi_2(\zeta) = \sum_{k=0}^{\infty} a_k \zeta^k + \sum_{k=1}^{\infty} b_k \zeta^{-k} \\ \psi_2(\zeta) = \sum_{k=0}^{\infty} c_k \zeta^k + \sum_{k=1}^{\infty} d_k \zeta^{-k} \end{cases} \tag{66}$$

where a, b, c, and d are all constants, which can be determined by the boundary function of the region where S_2 is located. Similarly, the stress function of the S_1 region can be obtained:

$$\begin{cases} \varphi_3(\zeta) = \sum_{k=0}^{\infty} A_k \zeta^k + \sum_{k=1}^{\infty} B_k \zeta^{-k} \\ \psi_3(\zeta) = \sum_{k=0}^{\infty} C_k \zeta^k + \sum_{k=1}^{\infty} D_k \zeta^{-k} \end{cases} \tag{67}$$

where A, B, C, and D are all constants, which can be determined by the boundary function of the region where S_1 is located.

Considering the CAES, when storing air, the temperature in the area where S_1 is located will rise, and under the action of heat conduction, the temperature at positions S_2 and S_3 will also rise. The complex elastic displacements of S_1, S_2, and S_3 under the influence of temperature [25] can be expressed as:

$$2G\left(u_\rho + \mathrm{i}u_\theta\right) = \frac{\bar{\zeta}}{\rho}\frac{\omega'(\zeta)}{|\omega(\zeta)|}\left[\kappa\varphi(\zeta) - \frac{\omega(\zeta)}{\overline{\omega'(\zeta)}}\overline{\varphi'(\zeta)} - \overline{\psi(\zeta)}\right] + 2G\frac{\bar{\zeta}}{\rho}\frac{\overline{\omega'(\zeta)}}{|\omega(\zeta)|}\omega(\zeta)\varepsilon \tag{68}$$

where $\varepsilon = \frac{1}{3}\Delta V$, δV is the change of unit volume in the mapping area under the action of thermal stress.

For S_1, if the internal boundary of the chamber is subjected to the gas load q, there are:

$$\varphi_3(t_1) + \frac{\omega(t_1)}{\overline{\omega'(t_1)}}\overline{\varphi_3'(t_1)} + \overline{\psi_3(t_1)} = q \tag{69}$$

The outer boundary of S_1 is in contact with S_2, and the deformation displacement consistency condition needs to be met:

$$\begin{aligned} &\frac{\kappa_2}{2G_2}\varphi_2(t_2) - \frac{1}{2G_2}\left(\frac{\omega(t_2)}{\overline{\omega'(t_2)}}\overline{\varphi_2'(t_2)} + \overline{\psi_2(t_2)}\right) + \omega_2(\zeta)\varepsilon_2 \\ =&\frac{\kappa_3}{2G_3}\varphi_3(t_2) - \frac{1}{2G_3}\left(\frac{\omega(t_2)}{\overline{\omega'(t_2)}}\overline{\varphi_3'(t_2)} + \overline{\psi_3(t_2)}\right) + \omega_3(\zeta)\varepsilon_3 \end{aligned} \tag{70}$$

At the same time, the contact between the outer boundary of S_1 and S_2 also needs to satisfy the condition of consistent force transmission:

$$\varphi_2(t_2) + \frac{\omega(t_2)}{\overline{\omega'(t_2)}}\overline{\varphi_2'(t_2)} + \overline{\psi_2(t_2)} = \varphi_3(t_2) + \frac{\omega(t_2)}{\overline{\omega'(t_2)}}\overline{\varphi_2'(t_3)} + \overline{\psi_3(t_2)} \tag{71}$$

Similarly, the conditions for consistent displacement deformation and force transmission in the S_2 and S_3 regions can be obtained, as shown in Equations (72) and (73), respectively:

$$\begin{aligned}&\frac{\kappa_1}{2G_1}\varphi_1(t_1)-\frac{1}{2G_1}\left(\frac{\omega(t_1)}{\overline{\omega'(t_1)}}\overline{\varphi_1'(t_1)}+\overline{\psi_1(t_1)}\right)+\omega_1(\zeta)\varepsilon_1\\=&\frac{\kappa_2}{2G_2}\varphi_2(t_2)-\frac{1}{2G_2}\left(\frac{\omega(t_2)}{\overline{\omega'(t_2)}}\overline{\varphi_2'(t_2)}+\overline{\psi_2(t_2)}\right)+\omega_2(\zeta)\varepsilon_2\end{aligned}\tag{72}$$

$$\varphi_1(t_1)+\frac{\omega(t_1)}{\overline{\omega'(t_1)}}\overline{\varphi_1'(t_1)}+\overline{\psi_1(t_1)}=\varphi_2(t_2)+\frac{\omega(t_2)}{\overline{\omega'(t_2)}}\overline{\varphi_2'(t_2)}+\overline{\psi_2(t_2)}\tag{73}$$

where t_1, t_2, and t_3 in Equations (69) to (73) are points on the boundaries of mapping regions S_1, S_2, and S_3, respectively. If the stress functions are separately applied to the boundary conditions, the expansion form of Equation (69) is:

$$\begin{cases}\sum\limits_{k=0}^{\infty}A_k\rho^{2k-v}(k-v+1)L_{k-v+1}\sigma^v-\sum\limits_{k=1}^{\infty}B_k\rho^{-2k-v}(k+v-1)L_{-k-v+1}\sigma^v+\sum\limits_{k=1}^{\infty}\overline{A_k}\rho^{2k+v-2}kL_{k+v-1}\sigma^v-\\ \sum\limits_{k=1}^{\infty}\overline{B_k}\rho^{-2k+v-2}kL_{-k+v-1}\sigma^v-\sum\limits_{k=0}^{\infty}\overline{C_k}\rho^{-v}(k+v-1)L_{-k-v+1}\sigma^v+\sum\limits_{k=1}^{\infty}\overline{D_k}\rho^{-v}(k-v+1)L_{k-v+1}\sigma^v=\\ 2q\sum\limits_{k=0}^{\infty}L_k\rho^{2k-v}(k-v+1)L_{k-v+1}\sigma^v-2q\sum\limits_{k=1}^{\infty}L_{-k}\rho^{-2k-v}(k+v-1)L_{-k-v+1}\sigma^v-\\ q\sum\limits_{k=0}^{\infty}L_k\rho^{-v}(k+v-1)L_{-k-v+1}\sigma^v+q\sum\limits_{k=1}^{\infty}L_{-k}\rho^{-v}(k-v+1)L_{k-v+1}\sigma^v,\quad v=0,\ 1,\ 2,\ 3,\ \cdots,\\ \sum\limits_{k=0}^{\infty}A_k\rho^{2k+v}(k+v+1)L_{k+v+1}\sigma^{-v}-\sum\limits_{k=1}^{\infty}B_k\rho^{-2k+v}(k-v-1)L_{-k+v+1}\sigma^{-v}+\sum\limits_{k=1}^{\infty}\overline{A_k}\rho^{2k-v-2}kL_{k-v-1}\sigma^{-v}-\\ \sum\limits_{k=1}^{\infty}\overline{B_k}\rho^{-2k-v-2}kL_{-k-v-1}\sigma^{-v}-\sum\limits_{k=0}^{\infty}\overline{C_k}\rho^{v}(k-v-1)L_{-k+v+1}\sigma^{-v}+\sum\limits_{k=1}^{\infty}\overline{D_k}\rho^{v}(k+v+1)L_{k+v+1}\sigma^{-v}=\\ 2q\sum\limits_{k=0}^{\infty}L_k\rho^{2k+v}(k+v+1)L_{k+v+1}\sigma^{-v}-2q\sum\limits_{k=1}^{\infty}L_{-k}\rho^{-2k+v}(k-v-1)L_{-k+v+1}\sigma^{-v}-\\ q\sum\limits_{k=0}^{\infty}L_k\rho^{v}(k-v-1)L_{-k+v+1}\sigma^{-v}+q\sum\limits_{k=1}^{\infty}L_{-k}\rho^{v}(k+v+1)L_{k+v+1}\sigma^{-v},\quad v=0,\ 1,\ 2,\ 3,\ \cdots\end{cases}\tag{74}$$

The expansion form of Equation (70) is:

$$
\begin{cases}
\dfrac{\kappa_2}{G_2}\sum\limits_{k=0}^{\infty} a_k\rho^{2k-v}(k-v+1)L_{k-v+1}\sigma^v - \dfrac{\kappa_2}{G_2}\sum\limits_{k=1}^{\infty} b_k\rho^{-2k-v}(k+v-1)L_{-k-v+1}\sigma^v - \dfrac{1}{G_2}\sum\limits_{k=1}^{\infty}\overline{a_k}\rho^{2k+v-2}kL_{k+v-1}\sigma^v + \\
\dfrac{1}{G_2}\sum\limits_{k=1}^{\infty}\overline{b_k}\rho^{-2k+v-2}kL_{-k+v-1}\sigma^v + \dfrac{1}{G_2}\sum\limits_{k=0}^{\infty}\overline{c_k}\rho^{-v}(k+v-1)L_{-k-v+1}\sigma^v - \dfrac{1}{G_2}\sum\limits_{k=1}^{\infty}\bar{d}_k\rho^{-v}(k-v+1)L_{k-v+1}\sigma^v - \\
\dfrac{\kappa_3}{G_3}\sum\limits_{k=0}^{\infty} A_k\rho^{2k-v}(k-v+1)L_{k-v+1}\sigma^v + \dfrac{\kappa_3}{G_3}\sum\limits_{k=1}^{\infty} B_k\rho^{-2k-v}(k+v-1)L_{-k-v+1}\sigma^v + \dfrac{1}{G_3}\sum\limits_{k=1}^{\infty}\overline{A_k}\rho^{2k+v-2}kL_{k+v-1}\sigma^v - \\
\dfrac{1}{G_3}\sum\limits_{k=1}^{\infty}\overline{B_k}\rho^{-2k+v-2}kL_{-k+v-1}\sigma^v - \dfrac{1}{G_3}\sum\limits_{k=0}^{\infty}\overline{C_k}\rho^{-v}(k+v-1)L_{-k-v+1}\sigma^v + \dfrac{1}{G_3}\sum\limits_{k=1}^{\infty}\overline{D_k}\rho^{-v}(k-v+1)L_{k-v+1}\sigma^v = \\
-\varepsilon_2\sum\limits_{k=0}^{\infty} L_k\rho^{2k-v}(k-v+1)L_{k-v+1}\sigma^v + \varepsilon_2\sum\limits_{k=1}^{\infty} L_{-k}\rho^{-2k-v}(k+v-1)L_{-k-v+1}\sigma^v + \varepsilon_3\sum\limits_{k=0}^{\infty} L_k\rho^{2k-v}(k-v+1) \\
L_{k-v+1}\sigma^v - \varepsilon_3\sum\limits_{k=1}^{\infty} L_{-k}\rho^{-2k-v}(k+v-1)L_{-k-v+1}\sigma^v, \quad v=1,\ 2,\ 3,\ \cdots \\
\dfrac{\kappa_2}{G_2}\sum\limits_{k=0}^{\infty} a_k\rho^{2k+v}(k+v+1)L_{k+v+1}\sigma^{-v} - \dfrac{k_2}{G_2}\sum\limits_{k=1}^{\infty} b_k\rho^{-2k+v}(k-v-1)L_{-k+v+1}\sigma^{-v} \\
-\dfrac{1}{G_2}\sum\limits_{k=1}^{\infty}\overline{a_k}\rho^{2k-v-2}kL_{k-v-1}\sigma^{-v} + \dfrac{1}{G_2}\sum\limits_{k=1}^{\infty}\overline{b_k}\rho^{-2k-v-2}kL_{-k-v-1}\sigma^{-v} + \dfrac{1}{G_2}\sum\limits_{k=0}^{\infty}\overline{c_k}\rho^{v}(k-v-1)L_{-k+v+1}\sigma^{-v} \\
-\dfrac{1}{G_2}\sum\limits_{k=1}^{\infty}\overline{d_k}\rho^{v}(k+v+1)L_{k+v+1}\sigma^{-v} - \dfrac{\kappa_3}{G_3}\sum\limits_{k=0}^{\infty} A_k\rho^{2k+v}(k+v+1)L_{k+v+1}\sigma^{-v} + \dfrac{k_3}{G_3}\sum\limits_{k=1}^{\infty} B_k\rho^{-2k+v}(k-v-1) \\
L_{-k+v+1}\sigma^{-v} + \dfrac{1}{G_3}\sum\limits_{k=1}^{\infty}\overline{A_k}\rho^{2k-v-2}kL_{k-v-1}\sigma^{-v} - \dfrac{1}{G_3}\sum\limits_{k=1}^{\infty}\overline{B_k}\rho^{-2k-v-2}kL_{-k-v-1}\sigma^{-v} - \dfrac{1}{G_3}\sum\limits_{k=0}^{\infty}\overline{C_k}\rho^{v}(k-v-1) \\
L_{-k+v+1}\sigma^{-v} + \dfrac{1}{G_3}\sum\limits_{k=1}^{\infty}\overline{D_k}\rho^{v}(k+v+1)L_{k+v+1}\sigma^{-v} = -\varepsilon_2\sum\limits_{k=0}^{\infty} L_k\rho^{2k+v}(k+v+1)L_{k+v+1}\sigma^{-v} \\
+\varepsilon_2\sum\limits_{k=1}^{\infty} L_{-k}\rho^{-2k+v}(k-v-1)L_{-k+v+1}\sigma^{-v} + \varepsilon_3\sum\limits_{k=0}^{\infty} L_k\rho^{2k+v}(k+v+1)L_{k+v+1}\sigma^{-v} \\
-\varepsilon_3\sum\limits_{k=1}^{\infty} L_{-k}\rho^{-2k+v}(k-v-1)L_{-k+v+1}\sigma^{-v}, \quad v=0,\ 1,\ 2,\ 3,\ \cdots
\end{cases}
\tag{75}
$$

The expansion form of Equation (71) is:

$$
\begin{cases}
\sum\limits_{k=0}^{\infty} a_k \rho^{2k-v}(k-v+1)L_{k-v+1}\sigma^v - \sum\limits_{k=1}^{\infty} b_k \rho^{-2k-v}(k+v-1)L_{-k-v+1}\sigma^v + \sum\limits_{k=1}^{\infty} \overline{a_k}\rho^{2k+v-2}kL_{k+v-1}\sigma^v - \\
\sum\limits_{k=1}^{\infty} \overline{b_k}\rho^{-2k+v-2}kL_{-k+v-1}\sigma^v - \sum\limits_{k=0}^{\infty} \overline{c_k}\rho^{-v}(k+v-1)L_{-k-v+1}\sigma^v + \sum\limits_{k=1}^{\infty} \overline{d_k}\rho^{-v}(k-v+1)L_{k-v+1}\sigma^v - \\
\sum\limits_{k=0}^{\infty} A_k \rho^{2k-v}(k-v+1)L_{k-v+1}\sigma^v + \sum\limits_{k=1}^{\infty} B_k \rho^{-2k-v}(k+v-1)L_{-k-v+1}\sigma^v - \sum\limits_{k=1}^{\infty} \overline{A_k}\rho^{2k+v-2}kL_{k+v-1}\sigma^v + \\
\sum\limits_{k=1}^{\infty} \overline{B_k}\rho^{-2k+v-2}kL_{-k+v-1}\sigma^v + \sum\limits_{k=0}^{\infty} \overline{C_k}\rho^{-v}(k+v-1)L_{-k-v+1}\sigma^v \\
- \sum\limits_{k=1}^{\infty} \overline{D_k}\rho^{-v}(k-v+1)L_{k-v+1}\sigma^v = 0, \quad v = 0,\ 1,\ 2,\ 3,\ \cdots \\
\sum\limits_{k=0}^{\infty} a_k \rho^{2k+v}(k+v+1)L_{k+v+1}\sigma^{-v} - \sum\limits_{k=1}^{\infty} b_k \rho^{-2k+v}(k-v-1)L_{-k+v+1}\sigma^{-v} + \sum\limits_{k=1}^{\infty} \overline{a_k}\rho^{2k-v-2}kL_{k-v-1}\sigma^{-v} - \\
\sum\limits_{k=1}^{\infty} \overline{b_k}\rho^{-2k-v-2}kL_{-k-v-1}\sigma^{-v} - \sum\limits_{k=0}^{\infty} \overline{c_k}\rho^{v}(k-v-1)L_{-k+v+1}\sigma^{-v} + \sum\limits_{k=1}^{\infty} \overline{d_k}\rho^{v}(k+v+1)L_{k+v+1}\sigma^{-v} - \\
\sum\limits_{k=0}^{\infty} A_k \rho^{2k+v}(k+v+1)L_{k+v+1}\sigma^{-v} + \sum\limits_{k=1}^{\infty} B_k \rho^{-2k+v}(k-v-1)L_{-k+v+1}\sigma^{-v} - \sum\limits_{k=1}^{\infty} \overline{A_k}\rho^{2k-v-2}kL_{k-v-1}\sigma^{-v} + \\
\sum\limits_{k=1}^{\infty} \overline{B_k}\rho^{-2k-v-2}kL_{-k-v-1}\sigma^{-v} + \sum\limits_{k=0}^{\infty} \overline{C_k}\rho^{v}(k-v-1)L_{-k+v+1}\sigma^{-v} \\
- \sum\limits_{k=1}^{\infty} \overline{D_k}\rho^{v}(k+v+1)L_{k+v+1}\sigma^{-v} = 0, \quad v = 0,\ 1,\ 2,\ 3,\ \cdots
\end{cases}
\tag{76}
$$

The expansion form of Equation (72) is:

$$
\begin{cases}
\dfrac{\kappa_2}{G_2}\sum\limits_{k=0}^{\infty} a_k\rho^{2k-v}(k-v+1)L_{k-v+1}\sigma^v - \dfrac{\kappa_2}{G_2}\sum\limits_{k=1}^{\infty} b_k\rho^{-2k-v}(k+v-1)L_{-k-v+1}\sigma^v - \dfrac{1}{G_2}\sum\limits_{k=1}^{\infty}\overline{a_k}\rho^{2k+v-2}kL_{k+v-1}\sigma^v + \\
\dfrac{1}{G_2}\sum\limits_{k=1}^{\infty}\overline{b_k}\rho^{-2k+v-2}kL_{-k+v-1}\sigma^v + \dfrac{1}{G_2}\sum\limits_{k=0}^{\infty}\overline{c_k}\rho^{-v}(k+v-1)L_{-k-v+1}\sigma^v - \dfrac{1}{G_2}\sum\limits_{k=1}^{\infty}\bar{d}_k\rho^{-v}(k-v+1)L_{k-v+1}\sigma^v - \\
\dfrac{\kappa_1}{G_1}\sum\limits_{k=0}^{\infty} h_k\rho^{-2k-v}(k+v-1)L_{-k-v+1}\sigma^v - \dfrac{1}{G_1}\sum\limits_{k=0}^{\infty}\overline{h_k}\rho^{-2k+v-2}kL_{-k+v-1}\sigma^v \\
+\dfrac{1}{G_1}\sum\limits_{k=0}^{\infty} m_k\rho^{-v}(k-v+1)L_{k-v+1}\sigma^v = -\varepsilon_2\sum\limits_{k=0}^{\infty} L_k\rho^{2k-v}(k-v+1)L_{k-v+1}\sigma^v \\
+\varepsilon_2\sum\limits_{k=1}^{\infty} L_{-k}\rho^{-2k-v}(k+v-1)L_{-k-v+1}\sigma^v + \varepsilon_1\sum\limits_{k=0}^{\infty} L_k\rho^{2k-v}(k-v+1)L_{k-v+1}\sigma^v \\
-\varepsilon_1\sum\limits_{k=1}^{\infty} L_{-k}\rho^{-2k-v}(k+v-1)L_{-k-v+1}\sigma^v, \quad v=1,\ 2,\ 3,\ \cdots \\
\dfrac{\kappa_2}{G_2}\sum\limits_{k=0}^{\infty} a_k\rho^{2k+v}(k+v+1)L_{k+v+1}\sigma^{-v} - \dfrac{k_2}{G_2}\sum\limits_{k=1}^{\infty} b_k\rho^{-2k+v}(k-v-1)L_{-k+v+1}\sigma^{-v} \\
-\dfrac{1}{G_2}\sum\limits_{k=1}^{\infty}\overline{a_k}\rho^{2k-v-2}kL_{k-v-1}\sigma^{-v} + \dfrac{1}{G_2}\sum\limits_{k=1}^{\infty}\overline{b_k}\rho^{-2k-v-2}kL_{-k-v-1}\sigma^{-v} \\
+\dfrac{1}{G_2}\sum\limits_{k=0}^{\infty}\overline{c_k}\rho^{v}(k-v-1)L_{-k+v+1}\sigma^{-v} - \dfrac{1}{G_2}\sum\limits_{k=1}^{\infty}\overline{d_k}\rho^{v}(k+v+1)L_{k+v+1}\sigma^{-v} - \\
\dfrac{\kappa_1}{G_1}\sum\limits_{k=0}^{\infty} h_k\rho^{-2k+v}(k-v-1)L_{-k+v+1}\sigma^{-v} - \dfrac{1}{G_1}\sum\limits_{k=0}^{\infty}\overline{h_k}\rho^{-2k-v-2}kL_{-k-v-1}\sigma^{-v} \\
+\dfrac{1}{G_1}\sum\limits_{k=0}^{\infty} m_k\rho^{v}(k+v+1)L_{k+v+1}\sigma^{-v} = -\varepsilon_2\sum\limits_{k=0}^{\infty} L_k\rho^{2k+v}(k+v+1)L_{k+v+1}\sigma^{-v} \\
+\varepsilon_2\sum\limits_{k=1}^{\infty} L_{-k}\rho^{-2k+v}(k-v-1)L_{-k+v+1}\sigma^{-v} + \\
\varepsilon_1\sum\limits_{k=0}^{\infty} L_k\rho^{2k+v}(k+v+1)L_{k+v+1}\sigma^{-v} - \varepsilon_1\sum\limits_{k=1}^{\infty} L_{-k}\rho^{-2k+v}(k-v-1)L_{-k+v+1}\sigma^{-v}, \quad v=0,\ 1,\ 2,\ 3,\ \cdots
\end{cases}
\tag{77}
$$

The expansion form of Equation (73) is:

$$
\begin{cases}
\sum_{k=0}^{\infty} a_k \rho^{2k-v}(k-v+1)L_{k-v+1}\sigma^v - \sum_{k=1}^{\infty} b_k \rho^{-2k-v}(k+v-1)L_{-k-v+1}\sigma^v + \sum_{k=1}^{\infty} \overline{a_k}\rho^{2k+v-2}kL_{k+v-1}\sigma^v - \\
\sum_{k=1}^{\infty} \overline{b_k}\rho^{-2k+v-2}kL_{-k+v-1}\sigma^v - \sum_{k=0}^{\infty} \overline{c_k}\rho^{-v}(k+v-1)L_{-k-v+1}\sigma^v + \sum_{k=1}^{\infty} \overline{d_k}\rho^{-v}(k-v+1)L_{k-v+1}\sigma^v + \\
2\Gamma \sum_{k=0}^{\infty} L_k \rho^{2k-v}(k-v+1)L_{k-v+1}\sigma^v - 2\Gamma \sum_{k=1}^{\infty} L_{-k}\rho^{-2k-v}(k+v-1)L_{-k-v+1}\sigma^v - \\
\Gamma' \sum_{k=0}^{\infty} L_k \rho^{-v}(k+v-1)L_{-k-v+1}\sigma^v + \Gamma' \sum_{k=1}^{\infty} L_{-k}\rho^{-v}(k-v+1)L_{k-v+1}\sigma^v, \quad v = 0,\ 1,\ 2,\ 3,\ \cdots \\
\sum_{k=0}^{\infty} a_k \rho^{2k+v}(k+v+1)L_{k+v+1}\sigma^{-v} - \sum_{k=1}^{\infty} b_k \rho^{-2k+v}(k-v-1)L_{-k+v+1}\sigma^{-v} + \sum_{k=1}^{\infty} \overline{a_k}\rho^{2k-v-2}kL_{k-v-1}\sigma^{-v} - \\
\sum_{k=1}^{\infty} \overline{b_k}\rho^{-2k-v-2}kL_{-k-v-1}\sigma^{-v} - \sum_{k=0}^{\infty} \overline{c_k}\rho^{v}(k-v-1)L_{-k+v+1}\sigma^{-v} + \sum_{k=1}^{\infty} \overline{d_k}\rho^{v}(k+v+1)L_{k+v+1}\sigma^{-v} + \\
\sum_{k=0}^{\infty} h_k \rho^{-2k+v}(k-v-1)L_{-k+v+1}\sigma^{-v} + \sum_{k=0}^{\infty} \overline{h_k}\rho^{-2k-v-2}kL_{-k-v-1}\sigma^{-v} - \sum_{k=0}^{\infty} m_k \rho^{v}(k+v+1)L_{k+v+1}\sigma^{-v} = \\
2\Gamma \sum_{k=0}^{\infty} L_k \rho^{2k+v}(k+v+1)L_{k+v+1}\sigma^{-v} - 2\Gamma \sum_{k=1}^{\infty} L_{-k}\rho^{-2k+v}(k-v-1)L_{-k+v+1}\sigma^{-v} - \\
\Gamma' \sum_{k=0}^{\infty} L_k \rho^{v}(k-v-1)L_{-k+v+1}\sigma^{-v} + \Gamma' \sum_{k=1}^{\infty} L_{-k}\rho^{v}(k+v+1)L_{k+v+1}\sigma^{-v}, \quad v = 0,\ 1,\ 2,\ 3,\ \cdots
\end{cases}
\tag{78}
$$

By combining Equations (74) to (78), a series of linear equation systems can be obtained. Solving these equation systems yields unknown constant terms in Equations (63), (66) and (67). Finally, these analytical stress functions can be substituted into Equation (68) to obtain the corresponding analytical solutions.

6. Verification a three-layer horseshoe shaped chamber

In Section 4.1, the analytical solution for the thermo-mechanical coupling of a three-layer horseshoe-shaped tunnel under steady-state conditions was derived. To validate the accuracy of the proposed solution, this section presents a comparative analysis with numerical simulations performed using COMSOL 6.2. The comparison is conducted through line graphs and contour plots, and the material parameters used remain consistent with those provided in Table 2.

Figure 9 illustrates the comparison between the analytical and numerical solutions for the horizontal and vertical directions of the tunnel at various temperatures. The selected temperatures for analysis include 25 °C, 50 °C, 75 °C, 100 °C, 150 °C, and 200 °C. Table 5 shows the relative errors, and it can be seen from the results that the analytical solution

obtained in this study is in good agreement with the FEM results. Although the numerical simulation results exhibit slightly higher values than the analytical solution, the discrepancy is minimal and can be considered negligible. This confirms the reliability and accuracy of the three-layer horseshoe-shaped tunnel analytical solution proposed in this study.

Table 5. Relative error analysis of analytical solutions and FEM results for horseshoe shaped chamber

Temperature	Horizontal temperature error (%)	Vertical temperature error (%)	Horizontal temperature error (%)	Vertical temperature error (%)
25 °C	0.193	0.501	8.646	1.044
50 °C	0.595	1.538	1.227	0.148
75 °C	0.734	1.896	0.753	0.089
100 °C	0.805	2.077	0.528	0.059
150 °C	0.876	2.259	0.314	0.036
200 °C	0.911	2.351	0.233	0.024

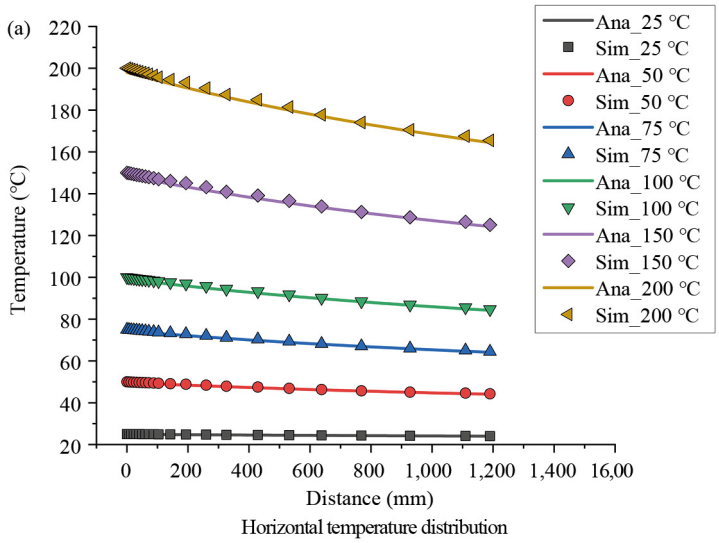

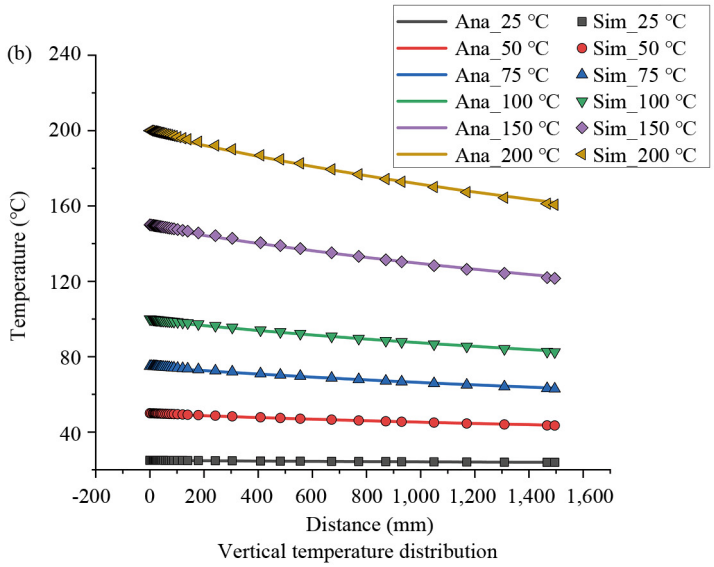

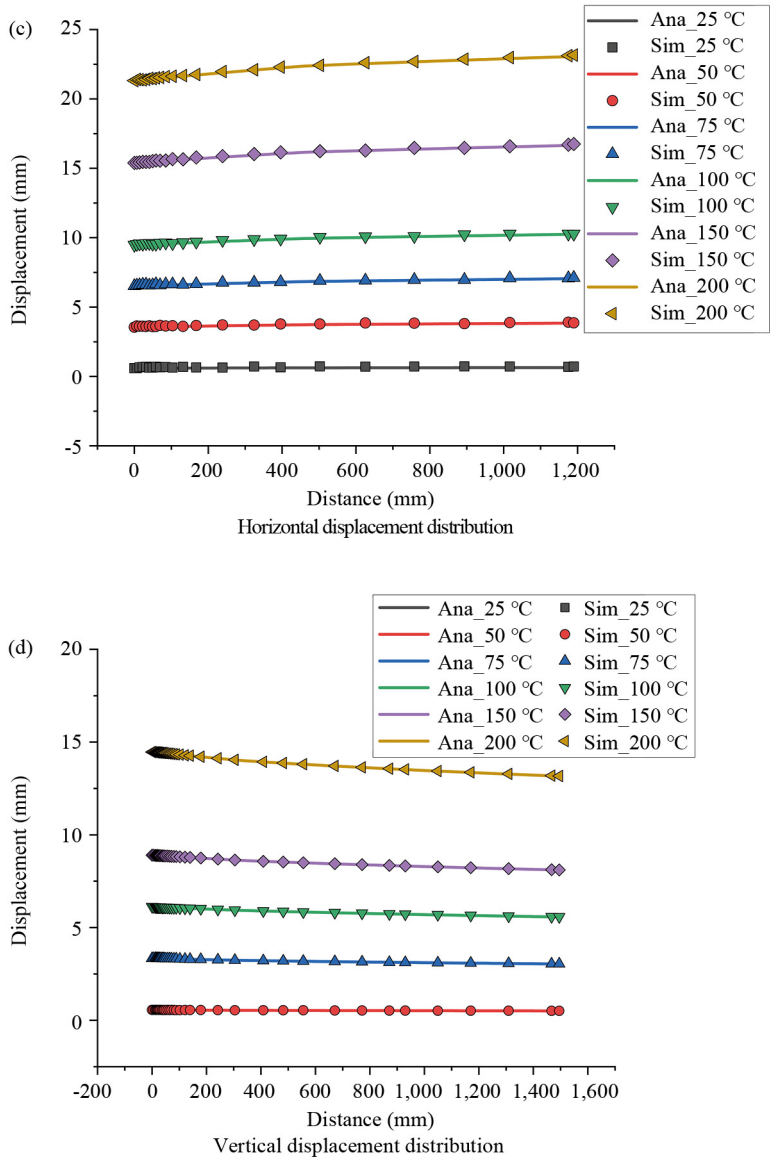

Figure 9. Comparison of analytical and finite element solutions

While Figure 9 provides a comparative analysis of the tunnel's horizontal and vertical responses, it does not fully depict the overall stress distribution. To address this, first principal stress contour maps are generated to evaluate the stress distribution at different burial depths and heights (100 m, 140 m, 180 m, 200 m, and 400 m) under a temperature of 75 °C, a lateral pressure coefficient of 1.5, and a chamber pressure of 8 MPa.

Figure 10 presents the temperature distributions obtained using the Finite Element Method (FEM) and the analytical solution. The comparison reveals that the temperature distributions in both cases are highly consistent, further validating the accuracy of the analytical approach. Additionally, Figures 11 compare the first principal stress contour maps at different burial depths. The comparison indicates that the two solutions exhibit strong agreement, confirming that the analytical solution remains applicable under general conditions and provides sufficient accuracy in capturing localized stress variations.

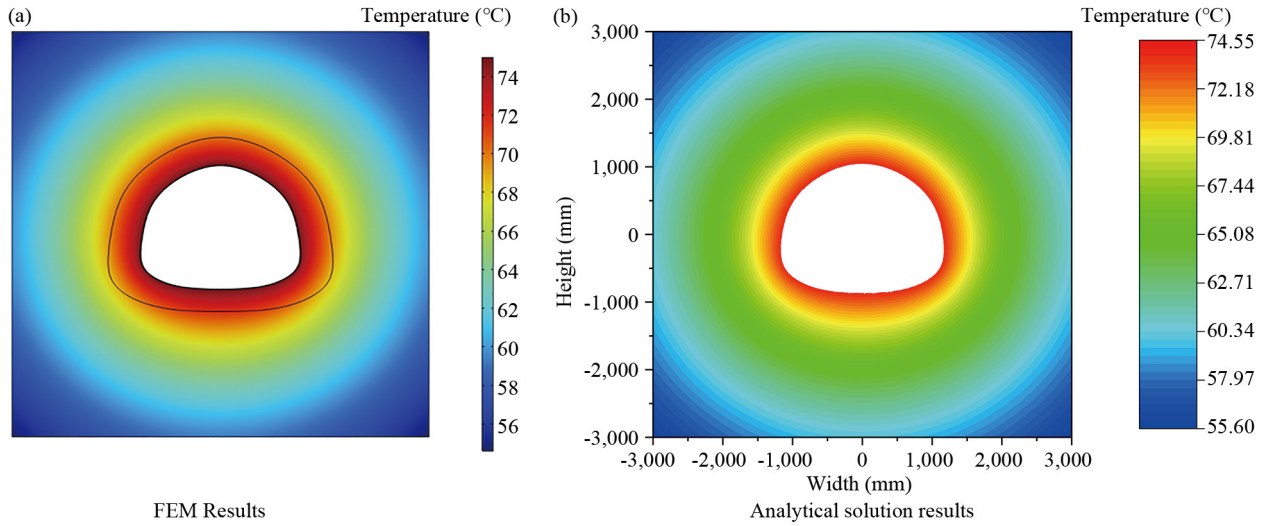

Figure 10. Comparison of temperature distributions at 75 °C

The results presented in Figure 10 and Figure 5 provide a comparative analysis of the first principal stress distributions in horseshoe-shaped and circular chambers under identical three-layer conditions. The comparison clearly demonstrates that stress distribution in horseshoe-shaped chambers is more complex and uneven compared to circular chambers.

According to the findings of Sun et al. [12], greater stress variations contribute to reduced tunnel stability and an increased likelihood of structural failure. The results indicate that horseshoe-shaped tunnels exhibit significantly larger stress concentrations, with local stress differences reaching up to 9 MPa. In contrast, circular tunnels experience lower stress variations, leading to improved structural stability. Consequently, from a stress distribution perspective, circular tunnels offer superior stability compared to their horseshoe-shaped counterparts.

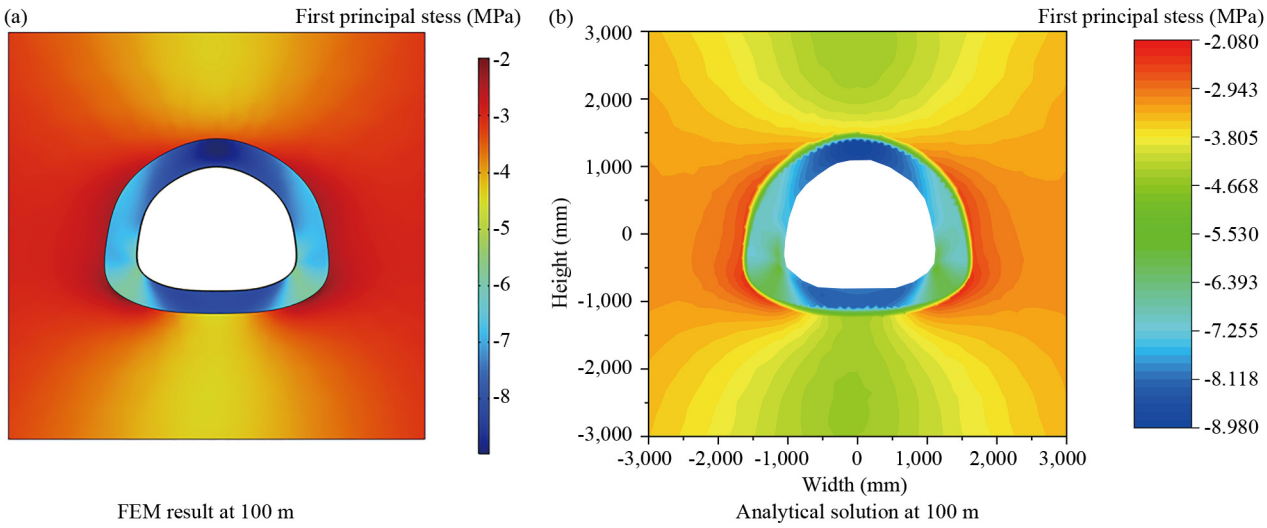

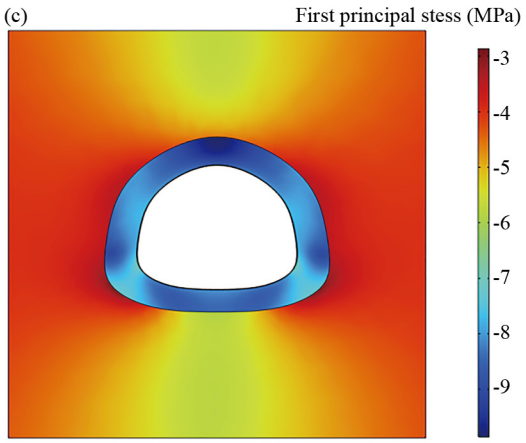

FEM result at 140 m

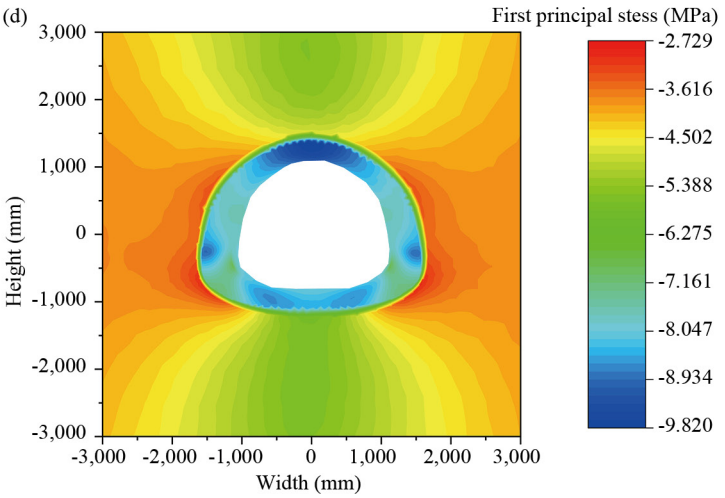

Analytical solution at 140 m

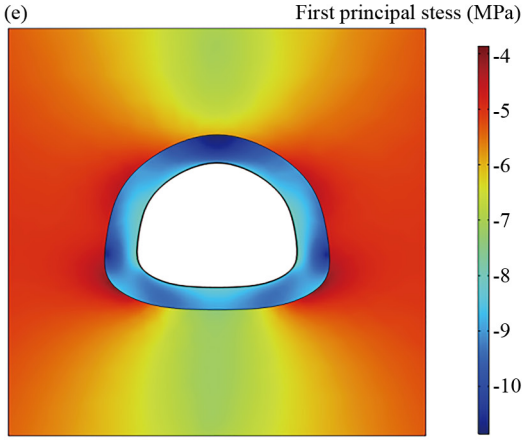

FEM result at 180 m

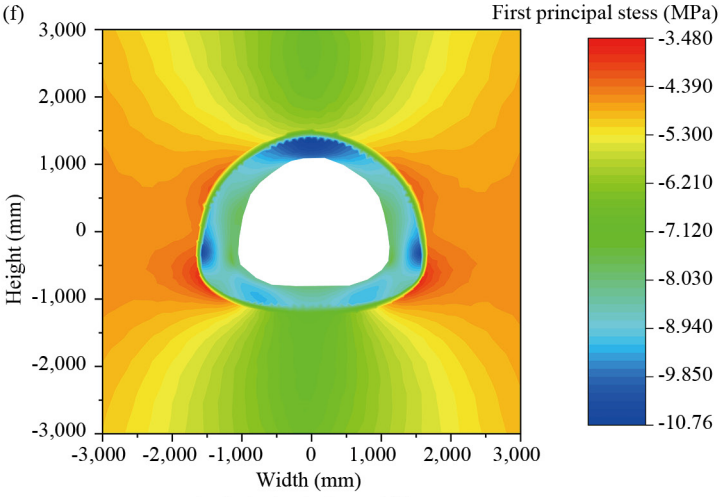

Analytical solution at 180 m

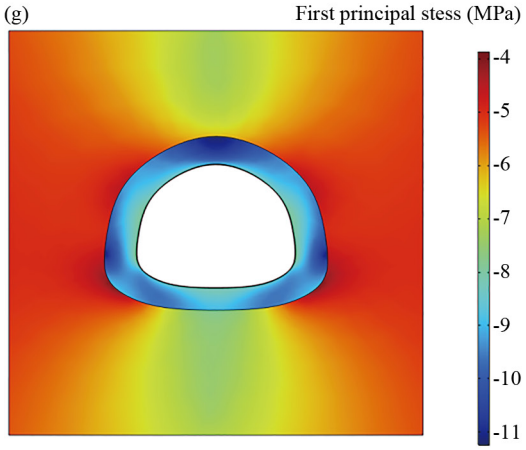

FEM result at 200 m

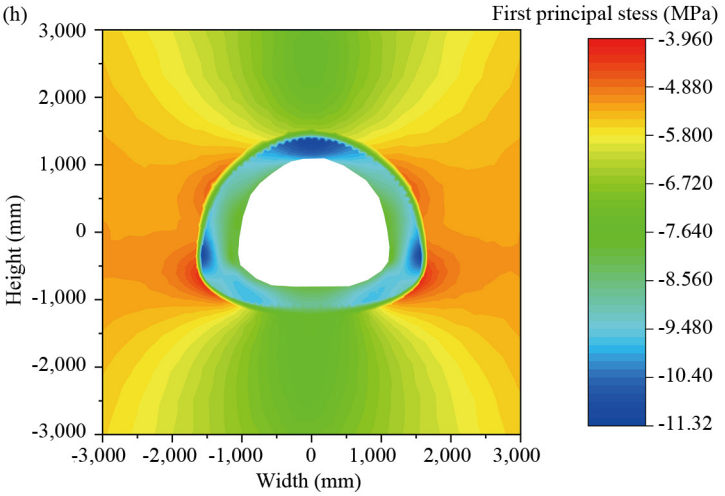

Analytical solution at 200 m

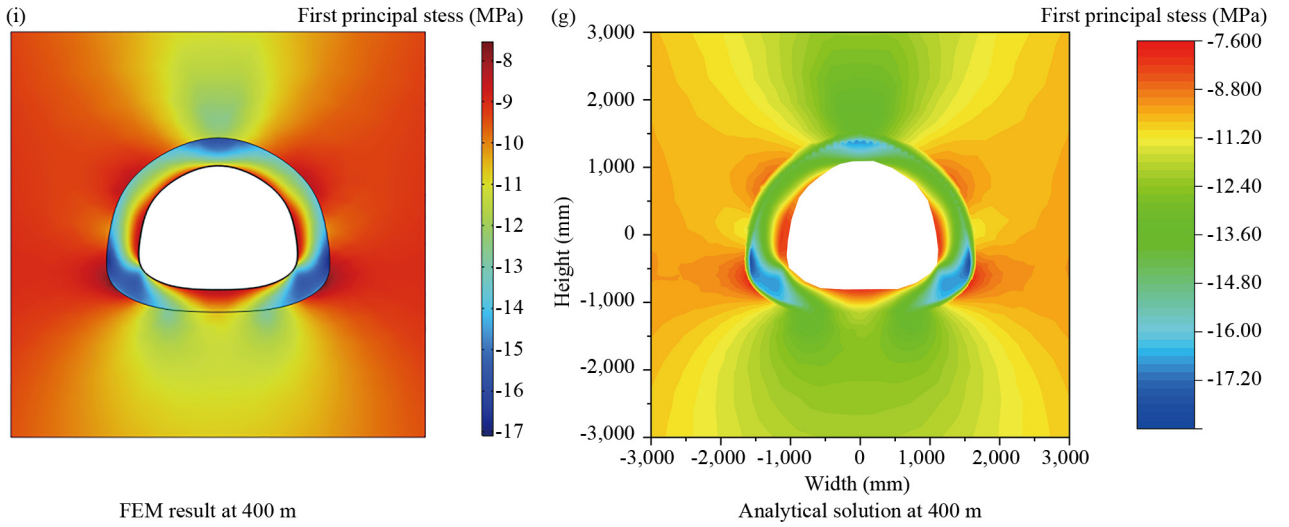

Figure 11. Comparison cloud map with finite element calculation results

7. Conclusions

In this study, an analytical framework was developed based on the fundamental assumptions of elasticity, incorporating both classical elasticity and complex elasticity under the influence of temperature. Utilizing this theoretical foundation, analytical solutions for both three-layer circular chambers and three-layer horseshoe-shaped chambers under steady-state heat conduction conditions were derived. To validate the accuracy of the theoretical model, the analytical solutions were compared with numerical results obtained from finite element simulations. The comparative analysis confirmed the reliability and accuracy of the proposed methodology. The research findings highlight the significant influence of temperature variations on the stress distribution and deformation of tunnel structures. The theoretical analysis and results presented in this study provide valuable insights for the design and optimization of CAES systems. The following key conclusions can be drawn:

(1) Analytical solution high precision and consistency with FEM

The analytical solution exhibits strong agreement with finite element results, confirming its validity and accuracy. The comparative analysis revealed that temperature changes play a crucial role in stress distribution within tunnels. Under high-temperature conditions, substantial thermal stress is generated on the inner surface of the tunnel, whereas the external temperature remains relatively stable. Due to their geometric characteristics, horseshoe-shaped chambers exhibit a more complex stress distribution compared to circular chambers.

(2) Application of complex elasticity and conformal transformation

By employing the theory of complex elasticity and conformal transformation, the challenge posed by the complex geometric shape of horseshoe-shaped chambers was successfully addressed, yielding high-precision analytical solutions. When $N = 8$, the tunnel shape derived from the mapping function closely matched the actual geometry, with an error margin of only 0.049%, demonstrating the effectiveness of the proposed transformation approach.

(3) Comparative structural stability of horseshoe-shaped and circular chambers

The stress distribution in horseshoe-shaped chambers is significantly more complex than that in circular chambers, exhibiting larger stress variations. As a result, horseshoe-shaped chambers are inherently less stable than their circular counterparts. Additionally, stress concentration is notably higher at the lower arch and corner regions of the horseshoe-shaped chamber, increasing the likelihood of structural failure.

These findings not only offer theoretical support for the design and optimization of CAES chambers but also provide engineering guidance for their practical implementation in repurposed underground environments. In particular, circular chambers are recommended for improved structural stability, while special reinforcement should be considered at stress concentration zones in horseshoe-shaped designs. The analytical framework developed in this study can serve as a fast and effective tool for early-stage design evaluation. Nonetheless, this work assumes steady-state thermal conditions and linear elastic material behavior, which may not fully capture the long-term performance under cyclic loading and varying environmental conditions. Future research should focus on incorporating transient thermal effects, nonlinear or time-dependent material properties, and interface behavior between different chamber layers.

Acknowledgements

This work is supported by the Fund of State Key Laboratory of Intelligent Construction and Healthy Operation and Maintenance of Deep Underground Engineering (Grant No. SDGZ2541), the National Natural Science Foundation of China (42307202), the Basic Research Program of Jiangsu (BK20221135, BK20243024), and the Young Elite Scientists Sponsorship Program by CAST (2023QNRC001).

Data availability

Data will be made available on request.

Conflict of interest

The authors declare that they have no known competing financial interests or personal relationships that could have appeared to influence the work reported in this paper.

References

[1] King M, Jain A, Bhakar R, Mathur J, Wang J. Overview of current compressed air energy storage projects and analysis of the potential underground storage capacity in India and the UK. *Renewable and Sustainable Energy Reviews*. 2021; 139: 110705. Available from: https://doi.org/10.1016/j.rser.2021.110705.

[2] Sun R, Wang J, Zhou Y, Shang X, Leung C. Stability analysis of a compressed air energy storage cavern transformed from a horseshoe-shaped roadway in an abandoned coal mine. *Deep Underground Science and Engineering*. 2025; 1-20. Available from: https://doi.org/10.1002/dug2.70041.

[3] Smdani G, Islam MR, Ahmad Yahaya AN, Bin Safie SI. Performance evaluation of advanced energy storage systems: A review. *Energy and Environment*. 2023; 34: 1094-1141. Available from: https://doi.org/10.1177/0958305X221074729.

[4] Liu X, Yang J, Yang C, Zhang Z, Chen W. Numerical simulation on cavern support of compressed air energy storage (CAES) considering thermo-mechanical coupling effect. *Energy*. 2023; 282: 128916. Available from: https://doi.org/10.1016/j.energy.2023.128916.

[5] Polański K. Influence of the variability of compressed air temperature on selected parameters of the deformation-stress state of the rock mass around a CAES salt cavern. *Energies*. 2021; 14: 6197. Available from: https://doi.org/10.3390/en14196197.

[6] Li H, Ma H, Liu J, Zhu S, Zhao K, Zheng Z, et al. Large-scale CAES in bedded rock salt: A case study in jiangsu province, china. *Energy*. 2023; 281: 128271. Available from: https://doi.org/10.1016/j.energy.2023.128271.

[7] Bazdar E, Sameti M, Nasiri F, Haghighat F. Compressed air energy storage in integrated energy systems: A review. *Renewable and Sustainable Energy Reviews*. 2022; 167: 112701. Available from: https://doi.org/10.1016/j.rser.2022.112701.

[8] Hu B, Yu L, Mi X, Xu F, Li S, Li W, et al. Comparative analysis of thermodynamic and mechanical responses between underground hydrogen storage and compressed air energy storage in lined rock caverns. *International Journal of Mining Science and Technology*. 2024; 34: 531-543. Available from: https://doi.org/10.1016/j.ijmst.2024.04.005.

[9] Colas E, Kukla PA, Amann F, Back S. Geological and mining factors influencing further use of abandoned coal mines-a multi-disciplinary workflow towards sustainable underground storage. *Journal of Energy Storage*. 2025; 108: 115101. Available from: https://doi.org/10.1016/j.est.2024.115101.

[10] Hu B, Mi X, Li YY, Li S, Li W, Wei C. Effects of cushion gas pressure and operating parameters on the capacity of hydrogen storage in lined rock caverns (LRC). *Renewable Energy*. 2024; 235: 121317. Available from: https://doi.org/10.1016/j.renene.2024.121317.

[11] Wang Z, Zhu Z, Zhou L, Wang M, Ma L, Nie F, et al. Dynamic mechanical properties and failure characteristics of layered composite rock containing a tunnel-shaped hole. *Theoretical and Applied Fracture Mechanics*. 2024; 129: 104217. Available from: https://doi.org/10.1016/j.tafmec.2023.104217.

[12] Sun R, Wang J, Zhang K, Li F, Ding X, Guo Q. Stress redistribution in a multilayer chamber for compressed air energy storage in abandoned coalmine: Elastic analytical insights and material choice. *Energy Science and Engineering*. 2023; 11: 4198-4223. Available from: https://doi.org/10.1002/ese3.1574.

[13] Jankowski M, Pałac A, Sornek K, Goryl W, Żołądek M, Homa M, et al. Status and development perspectives of the compressed air energy storage (CAES) technologies-a literature review. *Energies*. 2024; 17(9): 2064. Available from: https://doi.org/10.3390/en17092064.

[14] Polański K. CAES as a way for large-scale storage of surplus energy in Poland from renewable energy sources. *Energies*. 2025; 18: 803. Available from: https://doi.org/10.3390/en18040803.

[15] Kim HM, Rutqvist J, Ryu DW, Choi BH, Sunwoo C, Song WK. Exploring the concept of compressed air energy storage (CAES) in lined rock caverns at shallow depth: A modeling study of air tightness and energy balance. *Applied Energy*. 2012; 92: 653-667. Available from: https://doi.org/10.1016/j.apenergy.2011.07.013.

[16] Wang J, Lu K, Ma L, Wang J, Dooner M, Miao S, et al. Overview of compressed air energy storage and technology development. *Energies*. 2017; 10: 991. Available from: https://doi.org/10.3390/en10070991.

[17] Matos CR, Silva PP, Carneiro JF. Overview of compressed air energy storage projects and regulatory framework for energy storage. *Journal of Energy Storage*. 2022; 55: 105862. Available from: https://doi.org/10.1016/j.est.2022.105862.

[18] Li Y, Zhou H, Cong R, Rao T. Current status and prospects of advanced compressed air energy storage in China. *Frontiers in Energy Research*. 2025; 3(1): 48-55. Available from: https://doi.org/10.61784/fer3019.

[19] Luo X, Wang J, Dooner M, Clarke J, Krupke C. Overview of current development in compressed air energy storage technology. *Energy Procedia*. 2014; 62: 603-611. Available from: https://doi.org/10.1016/j.egypro.2014.12.423.

[20] Holst K, Huff G, Schulte RH, Critelli N. *Lessons From Iowa: Development of a 270 Megawatt Compressed Air Energy Storage Project in Midwest Independent System Operator: A Study for the Doe Energy Storage Systems Program*. USA: Sandia National Laboratories (SNL); 2012. Available from: https://doi.org/10.2172/1035330.

[21] Evans DJ. The geology, historical background, and developments in CAES. In: Hauer A. (ed.) *Advances in Energy Storage*. USA: John Wiley and Sons, Ltd; 2022. p.323-389. Available from: https://doi.org/10.1002/9781119239390.ch18.

[22] Xu Y, Zhou S, Xia C, Zhao H, Xue X. Three-dimensional thermo-mechanical analysis of abandoned mine drifts for underground compressed air energy storage: A comparative study of two construction and plugging schemes. *Journal of Energy Storage*. 2021; 39: 102696. Available from: https://doi.org/10.1016/j.est.2021.102696.

[23] Zhao H, Hao X. Risk assessment of zero-carbon salt cavern compressed air energy storage power station. *Journal of Cleaner Production*. 2024; 468: 143002. Available from: https://doi.org/10.1016/j.jclepro.2024.143002.

[24] Venkataramani G, Parankusam P, Ramalingam V, Wang J. A review on compressed air energy storage-A pathway for smart grid and polygeneration. *Renewable and Sustainable Energy Reviews*. 2016; 62: 895-907. Available from: https://doi.org/10.1016/j.rser.2016.05.002.

[25] Zhang X, Gao Z, Zhou B, Guo H, Xu Y, Ding Y, et al. Advanced compressed air energy storage systems: Fundamentals and applications. *Engineering*. 2024; 34: 246-269. Available from: https://doi.org/10.1016/j.eng.2023.12.008.

[26] Chen X, Wang JG. Stability analysis for compressed air energy storage cavern with initial excavation damage zone in an abandoned mining tunnel. *Journal of Energy Storage*. 2022; 45: 103725. Available from: https://doi.org/10.1016/j.est.2021.103725.

[27] Thongraksa A, Punya-in Y, Jongpradist P, Kim HM, Jamsawang P. Failure behaviors of rock masses around highly pressurized cavern: Initiation and modes of failure. *Tunnelling and Underground Space Technology*. 2021; 115: 104058. Available from: https://doi.org/10.1016/j.tust.2021.104058.

[28] Raju M, Kumar Khaitan S. Modeling and simulation of compressed air storage in caverns: A case study of the huntorf plant. *Applied Energy*. 2012; 89: 474-481. Available from: https://doi.org/10.1016/j.apenergy.2011.08.019.

[29] Winn K, Wong LNY, Alejano LR. Multi-approach stability analyses of large caverns excavated in low-angled bedded sedimentary rock masses in Singapore. *Engineering Geology*. 2019; 259: 105164. Available from: https://doi.org/10.1016/j.enggeo.2019.105164.

[30] Rutqvist J, Kim HM, Ryu DW, Synn JH, Song WK. Modeling of coupled thermodynamic and geomechanical performance of underground compressed air energy storage in lined rock caverns. *International Journal of Rock Mechanics and Mining Sciences*. 2012; 52: 71-81. Available from: https://doi.org/10.1016/j.ijrmms.2012.02.010.

[31] Perazzelli P, Anagnostou G. Design issues for compressed air energy storage in sealed underground cavities. *Journal of Rock Mechanics and Geotechnical Engineering*. 2016; 8: 314-328. Available from: https://doi.org/10.1016/j.jrmge.2015.09.006.

[32] Kushnir R, Dayan A, Ullmann A. Temperature and pressure variations within compressed air energy storage caverns. *International Journal of Heat and Mass Transfer*. 2012; 55: 5616-5630. Available from: https://doi.org/10.1016/j.ijheatmasstransfer.2012.05.055.

[33] Zhou SW, Xia CC, Du SG, Zhang PY, Zhou Y. An analytical solution for mechanical responses induced by temperature and air pressure in a lined rock cavern for underground compressed air energy storage. *Rock Mechanics and Rock Engineering*. 2015; 48: 749-770. Available from: https://doi.org/10.1007/s00603-014-0570-4.

[34] Xia C, Zhou Y, Zhou S, Zhang P, Wang F. A simplified and unified analytical solution for temperature and pressure variations in compressed air energy storage caverns. *Renewable Energy*. 2015; 74: 718-726. Available from: https://doi.org/10.1016/j.renene.2014.08.058.

[35] Zhou SW, Xia CC, Zhao HB, Mei SH, Zhou Y. Numerical simulation for the coupled thermo-mechanical performance of a lined rock cavern for underground compressed air energy storage. *Journal of Geophysical Engineering*. 2017; 14: 1382-1398. Available from: https://doi.org/10.1088/1742-2140/aa7bd9.

[36] Wu D, Wang JG, Hu B, Yang SQ. A coupled thermo-hydro-mechanical model for evaluating air leakage from an unlined compressed air energy storage cavern. *Renewable Energy*. 2020; 146: 907-920. Available from: https://doi.org/10.1016/j.renene.2019.07.034.

[37] Kirsch G. Die Theorie der Elastizität und die Bedürfnisse der Festigkeitslehre [The theory of elasticity and the needs of strength of materials]. *Zentralblatt des Vereins Deutscher Ingenieure [Central Journal of the Association of German Engineers]*. 1898; 42: 797-807.

[38] Lu A, Zeng X, Xu Z. Solution for a circular cavity in an elastic half plane under gravity and arbitrary lateral stress. *International Journal of Rock Mechanics and Mining Sciences*. 2016; 89: 34-42. Available from: https://doi.org/10.1016/j.ijrmms.2016.08.004.

[39] Wang MB, Li SC. A complex variable solution for stress and displacement field around a lined circular tunnel at great depth. *International Journal for Numerical and Analytical Methods in Geomechanics*. 2009; 33: 939-951. Available from: https://doi.org/10.1002/nag.749.

[40] El Naggar H, Hinchberger SD, Lo KY. A closed-form solution for composite tunnel linings in a homogeneous infinite isotropic elastic medium. *Canadian Geotechnical Journal*. 2008; 45: 266-287. Available from: https://doi.org/10.1139/T07-055.

[41] Exadaktylos GE, Liolios PA, Stavropoulou MC. A semi-analytical elastic stress-displacement solution for notched circular openings in rocks. *International Journal of Solids and Structures*. 2003; 40: 1165-1187. Available from: https://doi.org/10.1016/S0020-7683(02)00646-7.

[42] Exadaktylos GE, Stavropoulou MC. A closed-form elastic solution for stresses and displacements around tunnels. *International Journal of Rock Mechanics and Mining Sciences*. 2002; 39: 905-916. Available from: https://doi.org/10.1016/S1365-1609(02)00079-5.

[43] Guo H, Xu Y, Kang H, Guo W, Liu Y, Zhang X, et al. From theory to practice: Evaluating the thermodynamic design landscape of compressed air energy storage systems. *Applied Energy*. 2023; 352: 121858. Available from: https://doi.org/10.1016/j.apenergy.2023.121858.

[44] Ji W, Wang S, Wan J, Cheng S, He J, Shi S. Stability analysis of surrounding rock of multi-cavern for compressed air energy storage. *Advances in Geo-Energy Research*. 2024; 13: 169-175. Available from: https://doi.org/10.46690/ager.2024.09.03.

[45] Li F, Li F, Sun R, Zheng J, Li X, Shen L, et al. A study on the transient response of compressed air energy storage in the interaction between gas storage chambers and horseshoe-shaped tunnels in an abandoned coal mine. *Energies*. 2024; 17: 953. Available from: https://doi.org/10.3390/en17040953.

[46] Molotnikov V, Molotnikova A. *Theory of Elasticity and Plasticity: A Textbook of Solid Body Mechanics*. Cham: Springer International Publishing; 2021. Available from: https://doi.org/10.1007/978-3-030-66622-4.

[47] Wang MZ, Xu BX, Gao CF. Recent general solutions in linear elasticity and their applications. *Applied Mechanics Reviews*. 2008; 61(3): 030803. Available from: https://doi.org/10.1115/1.2909607.

[48] Shi H, Bai M. Plastic zone analysis of deep-buried, noncircular tunnel and application on the high-speed railway in the karst area. *Mathematical Problems in Engineering*. 2017; 2017: 9523267. Available from: https://doi.org/10.1155/2017/9523267.

[49] Qin S, Xia C, Zhou S. Air tightness of compressed air storage energy caverns with polymer sealing layer subjected to various air pressures. *Journal of Rock Mechanics and Geotechnical Engineering*. 2023; 15: 2105-2116. Available from: https://doi.org/10.1016/j.jrmge.2022.10.007.

[50] Toupin RA. Saint-venant's principle. *Archive for Rational Mechanics and Analysis*. 1965; 18: 83-96. Available from: https://doi.org/10.1007/BF00282253.

[51] Han Y, Cui H, Ma H, Chen J, Liu N. Temperature and pressure variations in salt compressed air energy storage (CAES) caverns considering the air flow in the underground wellbore. *Journal of Energy Storage*. 2022; 52: 104846. Available from: https://doi.org/10.1016/j.est.2022.104846.

[52] Setiawan NB, Zimmerman RW. A unified methodology for computing the stresses around an arbitrarily-shaped hole in isotropic or anisotropic materials. *International Journal of Solids and Structures*. 2020; 199: 131-143. Available from: https://doi.org/10.1016/j.ijsolstr.2020.03.022.

[53] Lu A, Zhang N, Kuang L. Analytic solutions of stress and displacement for a non-circular tunnel at great depth including support delay. *International Journal of Rock Mechanics and Mining Sciences*. 2014; 70: 69-81. Available from: https://doi.org/10.1016/j.ijrmms.2014.04.008.

[54] Lu A, Zhang N, Qin Y. Analytical solutions for the stress of a lined non-circular tunnel under full-slip contact conditions. *International Journal of Rock Mechanics and Mining Sciences*. 2015; 79: 183-192. Available from: https://doi.org/10.1016/j.ijrmms.2015.08.008.